

Evolution of a wave packet into vortex loops in a laminar separation bubble

By JONATHAN H. WATMUFF

MCAT Inc., NASA Ames Research Center, Moffett Field, CA 94035, USA

(Received 31 March 1998 and in revised form 8 March 1999)

A laminar boundary layer develops in a favourable pressure gradient where the velocity profiles asymptote to the Falkner & Skan similarity solution. Flying-hot-wire measurements show that the layer separates just downstream of a subsequent region of adverse pressure gradient, leading to the formation of a thin separation bubble. In an effort to gain insight into the nature of the instability mechanisms, a small-magnitude impulsive disturbance is introduced through a hole in the test surface at the pressure minimum. The facility and all operating procedures are totally automated and phase-averaged data are acquired on unprecedentedly large and spatially dense measurement grids. The evolution of the disturbance is tracked all the way into the reattachment region and beyond into the fully turbulent boundary layer. The spatial resolution of the data provides a level of detail that is usually associated with computations.

Initially, a wave packet develops which maintains the same bounded shape and form, while the amplitude decays exponentially with streamwise distance. Following separation, the rate of decay diminishes and a point of minimum amplitude is reached, where the wave packet begins to exhibit dispersive characteristics. The amplitude then grows exponentially and there is an increase in the number of waves within the packet. The region leading up to and including the reattachment has been measured with a cross-wire probe and contours of spanwise vorticity in the centreline plane clearly show that the wave packet is associated with the cat's eye pattern that is a characteristic of Kelvin–Helmholtz instability. Further streamwise development leads to the formation of roll-ups and contour surfaces of vorticity magnitude show that they are three-dimensional. Beyond this point, the behaviour is nonlinear and the roll-ups evolve into a group of large-scale vortex loops in the vicinity of the reattachment. Closely spaced cross-wire measurements are continued in the downstream turbulent boundary layer and Taylor's hypothesis is applied to data on spanwise planes to generate three-dimensional velocity fields. The derived vorticity magnitude distribution demonstrates that the second vortex loop, which emerges in the reattachment region, retains its identity in the turbulent boundary layer and it persists until the end of the test section.

1. Introduction

Separation can occur at the leading edge of a blunt plate, i.e. in the vicinity (or just downstream) of the stagnation region. Separated flows can also arise after a boundary layer has undergone significant development, at a position where there is a change of surface geometry, such as flow over a forward or backward facing step, or flow over a three-dimensional hump. Alternatively, a boundary layer forming on a smooth continuous surface may separate because of the application of an adverse pressure gradient (APG). Classification into these distinct groups is based

on consideration of the most likely source of disturbances leading to growth of instabilities in the detached layer. The present work is concerned with the latter group, i.e. two-dimensional laminar boundary layer separation caused by application of an APG on a smooth surface.

Despite many studies of separated and reattaching flows there is still relatively little known about the unsteady flow structure. The response of separated flows to small-amplitude two-dimensional disturbances is reasonably well understood in terms of linear stability theory. However the behaviour of large-amplitude disturbances and the response of separated flows to three-dimensional disturbances, are poorly understood, even in the simplest of geometries. The objective of the present study is to gain a better understanding of the unsteady aspects, i.e. the underlying physical mechanisms governing the growth of disturbances (which originate in the layer upstream of separation) and the onset of nonlinearity and the final stages where breakdown of the disturbances is associated with turbulent reattachment.

Separated flow often occurs near the leading edge of a two-dimensional airfoil at an angle of attack, and the behaviour of the separated region is an important consideration with respect to the stalling characteristics of the airfoil. Jones (1934) classified three basic types of stalling characteristics of two-dimensional airfoils. The first type is caused by separation near the trailing edge while the other two types of stall are associated with separation near the leading edge. Based on detailed boundary-layer measurements associated with stalling airfoils, McCullough & Gault (1951) suggest that the other two types of stall consist of (i) leading-edge stall, caused by an abrupt separation near the leading edge without subsequent reattachment, and (ii) thin-airfoil stall, consisting of a laminar separation near the leading edge, with a turbulent reattachment point that moves progressively rearward with increasing incidence. At high Reynolds numbers or at low incidence, the extent of the separation bubble created by the reattachment is typically small and of order 1% of the airfoil chord. However, with an increase in the angle of incidence or a reduction in the flow speed, a short bubble can burst leading to a long bubble, and eventually the shear layer may even fail to reattach, leading to a detached shear layer in which vortex shedding can occur. The change in the mode of the separation and reattachment can occur gradually or sharply depending on the type of airfoil.

Various parameters have been proposed for correlating the characteristics of separation bubbles. Many investigators, e.g. Thwaites (1949) and Curle & Skan (1957), have proposed boundary layer separation criteria based on the following pressure gradient parameter:

$$m = (\theta_s^2/\nu)(\partial U_1/\partial x)_s \quad (1.1)$$

where the subscript s refers to conditions at the separation point, θ is the momentum thickness of the layer, ν is the kinematic viscosity, U_1 is the free-stream velocity and x is the coordinate in the streamwise direction.

Gaster (1966) performed a study of laminar separation bubbles on a flat plate under a wide range of Reynolds numbers and pressure distributions. He proposed an improved scaling for predicting the formation of long or short bubbles. Gaster argued that the fluid is practically stationary under the separated layer so the pressure gradient on the surface is almost zero. He suggested that the pressure gradient parameter should be based on the unseparated potential flow. Based on these arguments, he proposed two parameters for scaling the bursting of short bubbles, i.e. the Reynolds number based on the momentum thickness at the separation point and a modified pressure gradient parameter, $(\theta_s^2/\nu)(\Delta U_1/\Delta x)$, where ΔU_1 is the velocity difference based on

the unseparated potential flow over the length of the bubble, Δx . Gaster tripped the laminar layer to produce a fully attached turbulent boundary layer which enabled him to estimate ΔU_1 .

Two-dimensional separated flow contains a critical point and the linearized solution of the Navier–Stokes equations gives the angle, γ , between the surface and the separation streamline as

$$\tan \gamma = -3 \left(\frac{\partial \tau_o}{\partial x} \bigg/ \frac{dP}{dx} \right)_s, \quad (1.2)$$

where τ_o is the shear stress at the surface, e.g. see Lighthill (1963). Dobbinga, Ingen & Kooi (1972) investigated a wide variety of separated flows and proposed the following simple empirical relation for γ :

$$\tan \gamma = B/R_{\theta_s}, \quad (1.3)$$

where R_{θ_s} is the Reynolds number based on the momentum thickness at separation and B has values ranging from 15 to 20.

Observation of nominally two-dimensional (including axisymmetric) flows reveals an almost universal tendency to develop localized three-dimensional phenomena which can dominate the behaviour of the mean flow. Separated laminar flows are especially susceptible to this tendency. For example, almost invariably, three-dimensional cellular features are observed in the oil-flow pattern in the reattachment region behind a backward facing step, e.g. Roshko & Thomke (1966). It is less widely appreciated that similar three-dimensional cellular patterns also tend to occur for the case of separation and reattachment on a smooth continuous surface. A vivid example of three-dimensional cellular features for the case of a hemisphere-cylinder at zero angle of attack is visible in the oil-flow visualization studies of Peake & Tobak (1980). A laminar separation bubble in the form of an azimuthal ring can occur for the hemisphere-cylinder at zero angle of attack. This is the counterpart of the separation bubble that can form near the leading edge of a two-dimensional airfoil. The most striking feature of the oil-flow pattern shown by Peake & Tobak is the appearance of an almost equal azimuthal spacing between the cellular features in the reattachment region. The cause of these cellular features is unknown. One plausible explanation is that they arise from instabilities associated with three-dimensional disturbances which are present in the boundary layer upstream of the separation.

Laminar separated flows are inherently unstable, even at low Reynolds number, and the flow downstream of the reattachment is most often turbulent. In addition to the unsteadiness, the mean flow pattern is also dependent on instabilities that form in the separated flow, e.g. the length of the bubble is sensitive to the background disturbance level. Most prior investigations of laminar separation have been concerned with the mean flow structure, e.g. Gaster (1966) and Peake & Tobak (1980). The objective of the present study is to gain a better understanding of the underlying instability mechanisms.

The criterion used to classify the type of separation of the mean flow also serves to differentiate between the two mechanisms that lead to the formation of instabilities in separated flows. The first mechanism involves the generation of disturbances in the immediate vicinity of the change in the surface geometry, i.e. the step or hump. The second involves the transformation of disturbances evolving in the pre-separated layer into disturbances that are present in the separated flow, i.e. the receptivity of the boundary layer upstream of separation is important. Both mechanisms can be significant for the case where the separation is caused by local variations in the

surface geometry. However, in this case, it is more likely that a coupling will occur between the background (i.e. the environmental) disturbances and the appearance of instability waves in the separated flow, see Dovgal, Kozlov & Michalke (1994).

The present work is concerned with a nominally two-dimensional separation bubble, on a smooth flat surface, caused by application of an APG, i.e. disturbances which lead to the development of instabilities will originate upstream. In terms of the nomenclature used to describe the stalling characteristics of an airfoil, it will be shown that the separated flow considered in the present study has the characteristics of a short bubble.

One of the few investigations to focus on the details of the unsteady motions associated with separation bubbles was performed by Pauley, Moin & Reynolds (1990). They conducted a two-dimensional numerical investigation of the boundary layer separation on the floor of a duct caused by an APG introduced by suction through a port in the ceiling. The inflow boundary condition was the Blasius boundary layer. The steady-state solution without suction was used as the initial condition and the APG was applied impulsively at the start of the computation. A steady closed separation bubble was observed when the APG was relatively weak. As the strength of the APG was increased, the length of the separated region increased, oscillations developed in the skin friction observed at a fixed point and eventually periodic vortex shedding from the bubble was found to occur. The Strouhal number, based on the shedding frequency, local free-stream velocity and the momentum thickness of the layer at separation, was found to be independent of the Reynolds number and the pressure gradient. They showed that the shedding frequency was the same as that predicted by inviscid linear stability theory using parameters derived from the velocity distribution in the separated shear layer.

Based on comparisons with Gaster's results, Pauley *et al.* (1990) suggest that 'bursting' of a short separation bubble actually corresponds to the demise of unsteady separation. It is unfortunate that the term 'bursting' was originally established in the literature for describing the transformation from short to long separation bubbles. More recently, the term bursting has been used to describe the onset (rather than the demise) of unsteady phenomena such as those occurring in the transition from laminar to turbulent flow.

Pauley (1994) investigated the effects of three-dimensional disturbances introduced into the two-dimensional mean flow configuration of Pauley *et al.* (1990). The case of a random and a harmonic disturbance were considered separately. In both cases, the spanwise variations were amplified in the separation region and within the vortices shed from the bubble. However the vortex shedding frequency was unchanged from the two-dimensional case. The random perturbation appeared to have no observable effect on the spanwise structure, i.e. the length of the bubble and the strength of the shed vortices were the same as for the two-dimensional case when the velocity field was averaged across the span. However, the harmonic disturbance was found to increase the length of the separated bubble and it reduced the strength of the shed vortex. The harmonic disturbance was imposed across the span with an amplitude of 0.2% of the free-stream velocity and only a single spatial distribution was considered, i.e. the wavelength was half the width of the computational domain. Contours of the spanwise velocity had the appearance of streamwise vortices and Pauley suggested this was due to the formation of Görtler vortices, which is consistent with the work of Inger (1987).

The spatially distributed disturbances studied by Pauley are more complex than the case of a three-dimensional disturbance originating at a point. An example of

this simpler case is given in the landmark work of Gaster & Grant (1975) who used an impulsive disturbance at a point to generate a wave packet in a Blasius boundary layer. Gaster (1975) argued that the impulsive disturbance would excite all possible instability modes and that the wave packet forms through selective amplification and interference of these waves. He modelled the wave packet as a summation over all spanwise wavenumbers and frequencies of least-damped linear stability modes. He was able to reproduce (at least qualitatively) both the growth and structure of the wave packet observed by Gaster & Grant, by calculating the amplitude of each mode as it travelled downstream.

Investigations of the stability characteristics of a nominally two-dimensional separation bubble formed on the smooth surface of a two-dimensional airfoil are described in the reviews by Kozlov (1984) and Dovgal, Kozlov & Simonov (1986). They considered two-dimensional disturbances created by 100 dB sound intensity generated by a loudspeaker located in the diffuser of the tunnel and a vibrating ribbon located within the layer in the favourable pressure gradient (FPG) region. They also considered a three-dimensional disturbance generated by a point source in the FPG. Under acoustic excitation, the two-dimensional waves only became noticeable in the APG and further downstream the growth rate practically coincided with the two-dimensional waves initiated by the vibrating ribbon. The point source measurements are particularly relevant to the study considered in this paper but unfortunately many of the experimental details are not clear. However one distinctive characteristic observed when the point source was applied, is that considerable distortion of the mean flow was found to occur within the bubble at locations far away from the immediate vicinity of the ensuing wave packet.

It is evident that an impulsive disturbance originating at a point is a powerful tool for exploring the stability characteristics of laminar flows. Following the work of Gaster & Grant, an impulsive point disturbance is used in the present study in an effort to gain insight into the underlying instability mechanisms occurring in the separated flow.

2. Apparatus and experimental technique

The layer develops on a 1 m wide flat aluminium plate forming the test-section floor of an open-return wind tunnel. The plate is supported above an optics table which also serves as an extremely flat and rigid mounting platform for a high-speed computer-controlled three-dimensional probe traverse. A flexible ceiling is contoured to produce the pressure distribution and two Plexiglas sidewalls complete the test section. A scaled side view of the test section is shown in figure 1.

The pressure distribution is essentially the same as that used by Spalart & Watmuff (1993), which was specifically designed to create a *turbulent* boundary layer with a high enough Reynolds number to sustain the turbulence and allow accurate experimental measurements, but low enough for direct numerical simulation (DNS). The design incorporates a region of FPG, just downstream of the trip wire to let the turbulent boundary layer develop without unduly increasing the local Reynolds number. The APG is then applied rapidly. The APG is only moderate (i.e. the turbulent pressure gradient parameter, $\beta \approx 2$) and the turbulent layer of Spalart & Watmuff remains attached. Removal of the trip wire, while maintaining the same contoured ceiling shape and the same inlet unit Reynolds number leads to a *laminar* boundary layer, which separates in the APG and reattaches about 0.26 m downstream of the pressure minimum.

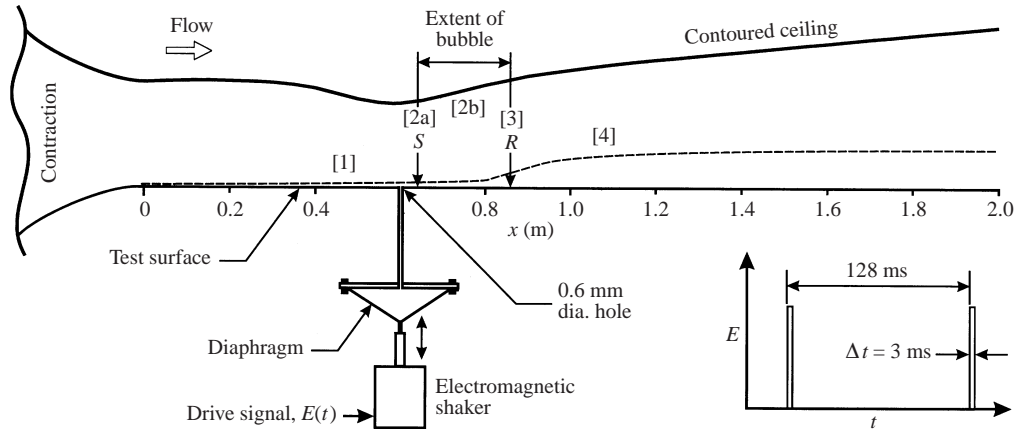


FIGURE 1. Scaled side view of 1 m wide test section with schematic showing the method for introduction of an impulsive disturbance at the C_p minimum. Arrows labelled S and R indicate the separation and reattachment points on the centreline without disturbance (from flying-hot-wire results, figure 5a). -----, 99% boundary layer thickness. Labels [1]–[4] refer to flow regimes.

The centreline pressure coefficient distributions for the laminar layer and the fully turbulent layer of Spalart & Watmuff are shown in figure 2. The pressure coefficient is defined as

$$C_p(x) = \frac{P(x) - P_{\text{ref}}}{P_{\text{tot}} - P_{\text{ref}}}, \quad (2.1)$$

where $P(x)$ is the static pressure measured with 0.6 mm diameter pressure taps located on the centreline of the test plate, and P_{tot} and P_{ref} are the total and static pressures measured with a Pitot-static tube located 0.1 m downstream of the exit of the contraction. Additionally, the velocity measured with the Pitot-static tube is used for the calibration of the hot-wire probes and for feedback while adjusting the tunnel speed to maintain the reference unit Reynolds number.

All pressures are measured using a MKS Baratron 398H differential pressure transducer with a range of 133 Pa and a 270 B signal conditioner. The pressures from a traversing Pitot tube, the 44 static wall tapings, and the reference Pitot-static tube are connected to the transducer via a 48-port Scanivalve pressure switch operated under computer control. A pause of 5 s is allowed for decay of transients after switching to the desired port and the average reading is obtained over a period of at least 30 s. The transducer contains a heating element that keeps the sensor at an approximately constant temperature in an effort to minimize drift with temperature. The reading obtained by connecting the same reference pressure across the transducer is used to monitor the transducer drift and it has been found to be almost non-existent. Nevertheless, as a precaution, this reading is always measured and then subtracted from each measurement.

Dantec 55P05 normal- and 55P51 cross-wire probes have been modified by reducing the prong separation and stiffening the prongs with the addition of a small web. Wollastan wire is soldered to the prongs and etched to produce filaments 2.5 μm in diameter and with an active length of 0.5 mm. The distance between the cross-wire filaments is 0.2 mm. The same normal- and cross-wire filaments have been used for all the measurements presented in this paper.

Perry, Lim & Henbest (1987) found substantial differences between profiles of the Reynolds shear stress measured in a rough-wall boundary layer where the turbulence

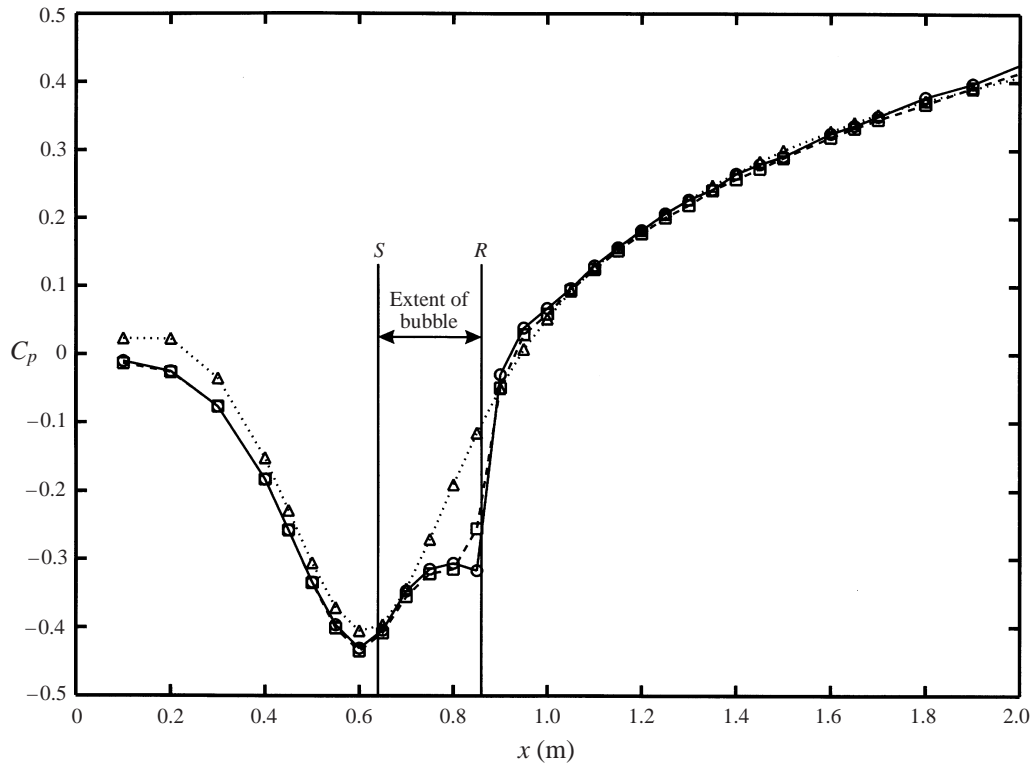


FIGURE 2. Centreline pressure distribution for two conditions in a laminar separation bubble study: \square , with disturbance; \circ , without disturbance. Lines S and R indicate separation and reattachment points without disturbance. Also shown is the distribution for a turbulent layer, tripped in a FPG, which does not separate: \triangle , Spalart & Watmuff (1993).

intensities are large compared to the mean velocity. The differences were found to depend on the included angle between the cross-wire filaments and on whether the probe was stationary or 'flying' upstream. The differences between the stationary and flying results were substantial for conventional probes where the included angle is nominally 90° . Only small differences were observed when the included angle was increased to 120° . By tilting the probes in a uniform stream, Perry *et al.* found that a flow angle of 45° could be imposed on the probe with the 120° included angle without appreciable error, whereas the probe with 90° included angle started to show errors at flow angles as low as 20° . Since relatively high relative turbulence intensities are experienced in the reattachment region, the included angle between the cross-wire filaments was set to about 110° , which is the maximum possible angle in consideration of the probe geometry. Use of this angle will reduce the errors compared to the standard 90° configuration. However, histogram estimates of the probability density function of the instantaneous flow angle have not been measured in the present configuration and the probe tilting tests described by Perry *et al.* were not performed, so it is difficult to provide estimates of the magnitude of the errors in the cross-wire data, particularly in the general vicinity of the reattachment.

Wall distances for the hot-wire probes are set using the electrical contact of a needle with the test surface. The wall distance is calibrated by focusing a telescope on the filaments and their images in the test surface. The telescope is also used to

ensure accurate alignment of the filaments with respect to the test surface. When the cross-wire probe is aligned normal to the test surface (i.e. for U and V measurements), the distance is taken to be between the points where the filaments and their images appear to cross. When the cross-wire probe is aligned for U and W measurements, the distance is taken to be between the mid-points of the filaments and their images. The closest data point to the test surface is 0.2 mm for the normal wire, and 1.2 mm for cross-wires.

The wires are operated with Dantec 55M10 constant-temperature hot-wire anemometers at a nominal resistance ratio of 1.8. The anemometers are operated with a flat response for the feedback amplifier and the typical system response of 75 kHz is more than adequate for the measurements. A d.c. voltage is subtracted from the anemometer outputs and the resulting signals are amplified so that they lie between ± 10 V over the range of velocities to be experienced by the wires. The hot-wire signals are not filtered.

The unit Reynolds number based on the reference free-stream velocity (U_{ref}) is $4.28 \times 10^5 \text{ m}^{-1}$ (i.e. $U_{\text{ref}} \approx 6.5 \text{ m s}^{-1}$). The reference conditions were measured at frequent intervals during all measurements and the unit Reynolds number was set to within 0.5% following the measurement of each profile by adjusting the speed of the fan. The free-stream unsteadiness, at a position on the centreline, 0.1 m downstream of the entry to the test section is given by $u/U_{\text{ref}} \approx 0.001$ (where u is the r.m.s. velocity fluctuation). Spectral measurements of the signal from a normal hot wire indicate that about 90% of the free-stream unsteadiness occurs below a frequency of 10 Hz. The distribution is relatively uniform in this frequency band with the exception of a narrow concentration of energy in a region centred around the rotational speed of the fan (approximately 6 Hz). The energy level at the blade-passing frequency of the fan (approximately 72 Hz) is relatively small. The correlation between the signals from two normal hot-wire probes located in the free stream and displaced 0.25 m in the spanwise direction, indicates that nearly 50% of the energy of the free-stream unsteadiness is in the form of acoustic disturbances generated by the fan.

2.1. Automation of the experiment

A high-speed computer-controlled three-dimensional probe traverse is integrated with the test section. The size and repeatability of the measurement volume are 2000 ± 0.1 mm in the (streamwise) x -direction, 100 ± 0.05 mm in the y -direction (normal to the test surface) and $\pm 200 \pm 0.05$ mm in the (spanwise) z -direction. The maximum traversing speed in the x -direction is 1.5 m s^{-1} , which is sufficient for flying-hot-wire measurements in the region of reversed flow, see Watmuff, Perry & Chong (1983). A microVAX II computer is used to control tunnel speed, probe traversal and data acquisition. A high-speed 15-bit Tustin analogue-to-digital converter is used for double-buffered data acquisition and processing. Processing of data in real time is an important requirement for the experiment owing to the total quantity of raw data acquired, particularly for the phase-averaged measurements. Storage of raw data for post-experimental processing was considered to be impractical owing to the excessively large disk storage requirements. Therefore considerable time was spent optimizing the double-buffered data acquisition and processing algorithms so that the real-time processing did not introduce significantly longer run times, see Watmuff (1995). Briefly, two arrays are set aside in computer memory. Data are acquired and transferred to each array alternately. True double buffering allows previously acquired data that are stored in one array to be processed, while data are simultaneously acquired and transferred to the other array. High-speed algorithms for processing the

hot-wire data provide a system throughput of 75 k s^{-1} for normal wires and 25 k s^{-1} for cross-wires. These rates can be sustained indefinitely even though the calculations are performed in double precision. The hot-wire calibration and data processing algorithms are described in more detail in §2.3.

A considerable investment in both hardware and software has enabled all the experimental procedures to be totally automated. Redundant safety measures and error detection and recovery schemes are located at each stage throughout the code. Complex three-dimensional measurement grids can be designed and viewed ahead of time. Program execution may be interrupted, asynchronously, at any stage, for any purpose, such as modification of control variables or verification of hardware operation, and then continued without loss of continuity. At a higher level, hot-wire calibration drift is monitored at regular intervals and new calibrations are performed and the measurements are repeated (automatically) until the drift is within a specified tolerance (typically 0.5%). Operation of the facility has been refined to the point where experiments can be performed continuously for several weeks at a time without scheduled manual supervision.

2.2. Introduction of impulsive disturbance at a point for generation of the wave packet

As mentioned in the introduction, Gaster & Grant (1975) were among the first to measure the evolution of a three-dimensional wave packet in detail by deliberately introducing a small-amplitude impulsive disturbance into a Blasius boundary layer. The motivation for using an impulsive disturbance was to excite all possible instability modes, thereby leading to a wave packet formed through selective amplification and interference of the waves. Gaster (1975) treated the wave packet as a summation over all spanwise wavenumbers and frequencies of least-damped linear stability eigenmodes. He was able to reproduce both the growth and structure of the wave packet measurements by calculating the amplitude of each mode as it travelled downstream.

Following Gaster & Grant, a small-magnitude disturbance has been introduced into the layer considered in the present work. The objective is to gain some understanding of the instability mechanisms in the separation bubble. The disturbance is introduced at the C_p minimum, since this is a clearly defined reference point that is located upstream of the separation. The motivation for using an impulsive disturbance is the same as in the work of Gaster & Grant, i.e. to excite all modes followed by selective amplification in the separated region of interest. The disturbance is repetitively introduced through a 0.6 mm diameter static pressure tapping as shown schematically in figure 1. The electromagnetic shaker and diaphragm perform the same function as electric speakers that have been used in previous studies, i.e. the source of the acoustic disturbance. The frequency response of the shaker is of order 1.5 kHz. Unlike the material used for speaker cones, the diaphragm is completely impervious to air flow so there is not even a small mean flow into or out of the hole in the test surface due to a static pressure difference. The length of the pressure tubing connecting the diaphragm to the pressure tap is 25 mm.

For the impulsive disturbances used in wave packet and turbulent spot studies, it is common practice to start sampling at a fixed frequency, after waiting a certain period of time after the introduction of the disturbance, e.g. see Cohen, Breuer & Haritonidis (1991). A number of realizations are measured after which an ensemble average is obtained for each data point. The technique is based on the same principles as averaging on the basis of the phase of the disturbance cycle, e.g. Reynolds & Hussain (1972), Cantwell & Coles (1983) and Perry & Watmuff (1981). However, one major difference between this technique and the phase-averaging method is

that the waiting period and the duration of sampling (i.e. the number of samples) can be designed such that only the relevant information associated with the wave packet is captured at the downstream measurement points. Furthermore, the time interval between the introduction of successive disturbances need not be periodic and it can be made arbitrarily large to allow the flow to fully recover from transients introduced by the passage of the disturbance. The data processing and storage requirements can be minimized since measurements are not required of the quiescent velocities observed before the arrival of the disturbance and after the passage of the disturbance, leading up to the start of the next disturbance cycle. While the technique described above offers several benefits, the phase-averaging method has been used for the measurements presented in this paper instead. The implications and the reasons for using the phase-averaging method are discussed in more detail in §2.3.

Attempts to observe the final nonlinear breakdown of a wave packet into a turbulent spot in the Blasius boundary layer have not been successful, e.g. Cohen *et al.* (1991). One explanation for this lack of success is that there is considerable variance in the downstream position where the final nonlinear breakdown of the wave packet occurs. In order to minimize the spatial jitter, most experimental studies of turbulent spots have used rather large disturbances (e.g. an electric spark or a strong impulsive jet through a hole in the wall) to force the formation of the spot to occur close to the source of the disturbance. The measurements of Cantwell, Coles & Dimotakis (1978) suggest that a spot appears to consist essentially of one or two large eddies. However, flow visualization studies have demonstrated that a typical spot appears to consist of an array of vortex loops, e.g. Perry, Lim & Teh (1981). Apparently, the variance in the underlying detailed structure, from realization to realization, causes washout of the detailed motions. In many of these studies, natural spot formation was not observed when the disturbance was removed, e.g. in the study of Cantwell *et al.* (1978), the undisturbed layer remained laminar along the entire test section length. It is not certain whether spots generated by such large disturbances are representative of spots that develop from wave packets which are generated by much smaller disturbances.

Nearly all of the above difficulties, concerning the observation of the final nonlinear breakdown of a wave packet, do not turn out to be limiting factors in the present separation bubble study. One of the benefits of the separation bubble is that the nonlinear growth of the instabilities occurs within a very small range of streamwise positions. During the exploratory stage of the project, it was discovered that complex large-amplitude hot-wire signals could be generated in the vicinity of the reattachment in a very repetitive manner by applying a small-amplitude impulsive drive signal to the shaker. The repetitive nature of these complex large-amplitude waveforms in the reattachment region implied that phase-averaged data would not suffer from washout owing to phase jitter or dispersion. It became evident during these tests that the motions could be studied in great detail by obtaining measurements on spatially dense three-dimensional grids. Further downstream, in the boundary layer established after the reattachment, the hot-wire signals appeared to be fully turbulent and uncorrelated with the impulsive disturbance originating upstream. However, cursory measurements indicated that meaningful phase-averaged measurements could be obtained far downstream of the reattachment region, although the r.m.s. amplitude of the phase-averaged velocities in this vicinity was an order of magnitude smaller than in the proximity of the reattachment.

Another significant observation is that the amplitude of the disturbance could be made very small without diminishing the relative magnitude of the phase-averaged velocities in the wave packet observed downstream. This is an important consideration

since the observations obtained using small disturbance amplitudes are likely to be more representative of the type of instabilities originating from small-magnitude background disturbances that are present in the layer upstream of the separation. This is in contrast with the turbulent spot studies mentioned above, where large disturbances are introduced, which bypass known transition mechanisms.

At a fixed point upstream of the reattachment, the characteristics of the hot-wire signals were found to depend on the magnitude and the duration of the impulse used for the shaker drive signal and on the period between successive applications of the impulse. The effects of varying the magnitude and the duration of the impulse were found to be much the same, provided that they are both small. Linear behaviour was observed under these conditions, i.e. the magnitude of the velocity signature observed with a hot wire was the same, relative to small changes in either the magnitude or the duration of the impulse. Nonlinear behaviour was observed when either the magnitude or the duration of the impulse was large. For the present work, the magnitude and duration of the drive signal applied to the shaker have been made as small as possible, i.e. below this threshold, the electromagnetic shaker would not respond to the drive signal.

As mentioned previously, the phase-averaging technique is used for all measurements, i.e. data are sampled and sorted on the basis of the phase of the disturbance cycle and all phase intervals are processed for the data storage. While the use of all of the phase intervals leads to a larger data storage requirement, this disadvantage is offset by the simpler post-experimental sorting procedure that is used to assemble the data into groups corresponding to the entire measurement grid for each phase interval. Furthermore, the data processing algorithms described in §2.3 can only be given a precise meaning if all phases are processed and stored. The use of the phase-averaging method allows the Reynolds stress to be calculated and the distribution can be related to the large-scale motions in the reattachment region and in the downstream turbulent boundary layer.

The period between successive applications of the disturbance must be large enough to allow for recovery of the flow after the passage of the disturbance. However too large a period is undesirable because a larger number of phase intervals would be required to resolve the motions of interest and this would increase the quantity of stored data. Larger periods would also require a longer time for a given number of realizations of the disturbance and therefore increase the total experimental run time. A minimum period between successive applications of the disturbance was determined by examining the hot-wire signals at a number of representative points in the flow. The signals which required the longest time to recover from passage of the disturbance were observed at points in the vicinity of maximum shear, at a streamwise position corresponding to the start of the region of exponential growth of the disturbance amplitude, i.e. $x \approx 0.72$ m, as shown in figure 9. Small periods, e.g. 50 ms, did not provide sufficient time for the transients to decay and this altered the character of the signals, i.e. the structure of the flow. A period of 128 ms was finally selected for performing the detailed study. The signals were the same as those produced by using a much longer period between the impulses, e.g. 5 s, and this period allowed the same degree of flow recovery after the transient passage of the disturbance.

In the region of exponential decay and growth of the disturbance amplitude (see figure 9) the normal hot-wire signals indicate a dominant wave frequency of approximately 87 Hz and spectral measurements indicate that very little energy exists at frequencies corresponding to the higher harmonics. The period of the dominant wave frequency (11.5 ms) corresponds to about 6 phase intervals which is sufficient

to resolve the individual waves within the packet. In the reattachment region, the streamwise spacing of the centreline cross-wire data is approximately $\frac{1}{15}$ of the streamwise extent of the cross-section through the emerging loops, i.e. the spatial resolution is more than adequate to determine the detailed motions.

2.3. Hot-wire calibration and data processing algorithms

The phase-averaging process assumes that a flow variable, S can be described by a global mean component, \bar{S} , a periodic component, \tilde{s} , and a random component, s'' . By definition, the total variable is given by the sum,

$$S = \bar{S} + \tilde{s} + s'' \quad (2.2a)$$

$$= \langle S \rangle + s'', \quad (2.2b)$$

where $\langle S \rangle$ represents the total phase-averaged component. This conforms with the notation used by Reynolds & Hussain (1972) and Cantwell & Coles (1983) with the exception of the nomenclature for the random component, s'' . The reason for the departure from their notation is to retain the conventional notation for decomposition of S into a temporal mean value, \bar{S} , and a random fluctuating component, s' , i.e.

$$S = \bar{S} + s'. \quad (2.3)$$

The drive signal applied to the shaker is sampled simultaneously with the hot-wire voltages. The leading edge of this signal is arbitrarily used to define the beginning of each phase cycle. Phase information is assigned to each sample using the relationship,

$$\phi = \left[\frac{I - I_j}{I_{j+1} - I_j} \right] N_\phi + 1, \quad I_j \leq I < I_{j+1}, \quad (2.4)$$

where I is the sample number to which phase information, ϕ , is to be assigned, I_j and I_{j+1} are the sample numbers corresponding to the start of the j th and $j + 1$ th disturbance cycles and N_ϕ is the number of phase intervals. For all measurements reported in the present work, $N_\phi = 64$. Phase information is assigned to measurements recorded before the first leading edge and after the last leading edge of the digitized drive-signal time record by using the average size of the phase interval.

Watmuff (1995) described a method for high-speed processing of cross-wire data in real time. The basis for the high speed is the assumption of simple cosine cooling for the heat transfer because the expression for the effective cooling velocity of each wire can then be reduced to a linear function of the applied velocity components. The calibration inversion is greatly simplified because the measurements are linearly dependent on the effective cooling velocity of each wire, which can be expressed uniquely in terms of the output voltage. This makes it practical to use a pair of one-dimensional look-up table arrays such that the number of elements corresponds exactly to the measurement resolution over the full range. This is the fastest possible method because the word returned by the analogue-to-digital converter can be used directly as the index of the look-up table array and linear interpolation is avoided. Watmuff showed that it is unnecessary to calculate U and V for each pair of cross-wire samples when only the mean flow, Reynolds stress and triple products are required and this further reduces the number of floating point calculations. The technique has been extended for the phase-averaged measurements reported in this paper and is outlined briefly below.

The effective cooling velocity of each wire can be expressed as functions $f_1(E_1)$

and $f_2(E_2)$ of the amplified anemometer output voltages E_1 and E_2 , i.e.

$$\begin{pmatrix} f_1 \\ f_2 \end{pmatrix} = \begin{pmatrix} \cos \psi_{e_1} & \sin \psi_{e_1} \\ \cos \psi_{e_2} & \sin \psi_{e_2} \end{pmatrix} \begin{pmatrix} U \\ V \end{pmatrix}, \quad (2.5)$$

where ψ_{e_1} and ψ_{e_2} are the effective wire angles, i.e. the angle between the normal to the wire filament and the streamwise direction, obtained by neglecting longitudinal cooling.

Although the method assumes simple cosine cooling, the difference (typically 2° or 3°) between the effective wire angle obtained by neglecting the longitudinal cooling component and the true wire angle, provides compensation. Watmuff (1995) used a Monte Carlo simulation to show that for moderate turbulence intensities (e.g. $u/\bar{U} = 20\%$) the errors are only slightly larger than the errors observed when the longitudinal cooling is fully accounted for.

An alternative formulation of (2.5) is given by

$$\begin{pmatrix} g_1 \\ g_2 \end{pmatrix} = \begin{pmatrix} 1 & \tan \psi_{e_1} \\ 1 & \tan \psi_{e_2} \end{pmatrix} \begin{pmatrix} U \\ V \end{pmatrix}, \quad (2.6)$$

where $g_1(E_1) = f_1(E_1)/\cos \psi_{e_1}$ and $g_2(E_2) = f_2(E_2)/\cos \psi_{e_2}$. The assumption of simple cosine cooling is vital for the high speed of the data reduction because the calibration inversion is then linear with respect to $g_1(E_1)$ and $g_2(E_2)$, i.e.

$$\begin{pmatrix} U \\ V \end{pmatrix} = \begin{pmatrix} 1 & \tan \psi_{e_1} \\ 1 & \tan \psi_{e_2} \end{pmatrix}^{-1} \begin{pmatrix} g_1 \\ g_2 \end{pmatrix}. \quad (2.7)$$

Another advantage of the formulation in (2.6) is that the functions $g_1(E_1)$ and $g_2(E_2)$ can be determined directly using a simple static calibration (i.e. with $V = W = 0$). In the present work, ten static calibration data points are used and least-squares cubic polynomials of best fit are determined for the effective cooling velocity as functions of $g_1(E_1)$ and $g_2(E_2)$. The polynomials have been found to fit the static calibration data to better than 0.5%.

Estimates of $\tan \psi_{e_1}$ and $\tan \psi_{e_2}$ are determined by oscillating the probe in the cross-stream direction after each static calibration point measurement. Using the high-speed traverse motors for this purpose means that additional special-purpose hardware is not required, e.g. for tilting the probes. A voltage proportional to the cross-stream traverse speed is derived from the motor step pulses. The wire and motor speed voltages are sampled on the basis of the position of the motor and $\tan \psi_{e_1}$ and $\tan \psi_{e_2}$ are obtained from least-squares lines of best fit applied to the perturbations of $g_1(E_1)$ and $g_2(E_2)$ as functions of the motor velocity. Almost no positional-dependent hysteresis could be found in the effective cooling velocity perturbations and the effective wire angles were found to be essentially independent of the free-stream velocity. Further details of the method can be found in Watmuff (1995). For the earlier cross-wire measurements, the effective wire angles were determined from the average of each static calibration point value. For later measurements, the probe oscillations to determine the effective wire angle were only performed at the largest free-stream calibration velocity.

The data in the centreline plane were measured using only the UV -orientation of the cross-wire probe. Measurements in cross-stream planes and for the three-dimensional grid were performed twice: once using the UV -orientation, and again using the UW -orientation of the cross-wire probe. The global mean velocities, \bar{U} and \bar{V} (or \bar{W}) and the total Reynolds stress components, $\overline{u^2}$, $\overline{u'v'}$ and $\overline{v'^2}$ (or $\overline{u'w'}$ and $\overline{w'^2}$),

were evaluated in double precision from running totals using all samples, i.e. $\sum g_1$, $\sum g_2$, $\sum g_1^2$, $\sum g_1 g_2$ and $\sum g_2^2$. An overbar applied to a time series implies a temporal mean value. Arrays of dimension N_ϕ are used to store running totals of $\sum g_{1\phi}$ and $\sum g_{2\phi}$ corresponding to each phase interval, ϕ . The total number of samples in each phase interval is stored in an integer array to enable calculation of the phase-averaged velocities $\langle U \rangle$ and $\langle V \rangle$ (or $\langle W \rangle$). The phase-averaged velocity perturbations \tilde{u} and \tilde{v} (or \tilde{w}) are determined by subtracting the global mean velocity components. The Reynolds stress components at constant phase are given by \tilde{u}^2 , $\tilde{u}\tilde{v}$ and \tilde{v}^2 (or $\tilde{u}\tilde{w}$ and \tilde{w}^2). The *contribution* to the total Reynolds stress by the phase-averaged velocities is defined in the present work as the average over all phases, i.e. $\overline{\tilde{u}^2}$, $\overline{\tilde{u}\tilde{v}}$ and $\overline{\tilde{v}^2}$ (or $\overline{\tilde{u}\tilde{w}}$ and $\overline{\tilde{w}^2}$). An overbar applied to phase-averaged quantities implies an average obtained over all phases. Running totals of $\sum g_{1\phi}^2$, $\sum g_{1\phi} g_{2\phi}$ and $\sum g_{2\phi}^2$ corresponding to each of the phase intervals are also stored for evaluation of the phase-averaged Reynolds stress components, i.e. $\langle u''^2 \rangle$, $\langle u''v'' \rangle$ and $\langle v''^2 \rangle$ (or $\langle u''w'' \rangle$ and $\langle w''^2 \rangle$). The contribution to the total Reynolds stress components by the random *background* fluctuations are defined by averaging over all phases, i.e. $\overline{\langle u''^2 \rangle}$, $\overline{\langle u''v'' \rangle}$ and $\overline{\langle v''^2 \rangle}$ (or $\overline{\langle u''w'' \rangle}$ and $\overline{\langle w''^2 \rangle}$).

Similar methods are used for the normal hot-wire data except that lookup table values of velocity can be used directly (instead of the effective cooling velocities required for the cross-wires). The data are also processed in real time and the stored quantities consist of the global mean velocity and total Reynolds stress as well as the phase-averaged velocity and normal Reynolds stress corresponding to each phase interval.

It can be shown that the globally averaged Reynolds stress components are given by the sum of the contribution and the background components, e.g.

$$\overline{u'^2} = \overline{\tilde{u}^2} + \overline{\langle u''^2 \rangle}. \quad (2.8)$$

The ratio of the background component to the total Reynolds stress (such as $\overline{\langle u''^2 \rangle} / \overline{u'^2}$) provides a quantitative measure of the randomness in the flow. The background component of the Reynolds stress originates from two sources: (i) fluctuations due to small-scale random motions superimposed on the large-scale motions and (ii) dispersion, introduced by phase jitter and the physical differences between successive realizations.

In the present work the phase averages at each point are derived from 16 384 samples obtained at intervals corresponding to the $N_\phi = 64$ phase intervals used to describe each cycle, i.e. a population of 256 disturbance cycles for the ensemble averages for each phase interval. The 128 ms period between successive applications of impulse for the drive signal leads to a sampling frequency of 500 Hz and a total sampling period of 32.8 s at each data point. Both broadband and phase-averaged quantities are calculated in real time using the same raw hot-wire voltages.

2.4. Measurement grids

Compared to a cross-wire probe, a normal hot wire can be positioned closer to the wall, it has better spatial resolution, the effects of high shear are almost negligible, and it is less susceptible to error in regions of high turbulence intensity. Mean flow and broadband unsteadiness profiles have been measured with a normal hot wire at $\Delta x = 50$ mm intervals on the centreline along the entire test section. Phase-averaged normal hot-wire data have been measured on 42 spanwise planes at $\Delta x = 10$ mm intervals in the streamwise direction. The spanwise planes originate 10 mm upstream of the hole where the disturbance is introduced (i.e. $x = 0.59$ m).

Phase-averaged cross-wire data have been measured on four successive grids on the

centreline plane normal to the wall. The results from each grid have been combined to form a composite data set on a single grid consisting of $(N_x, N_y) = (250, 17)$, i.e. 4250 data points. The streamwise origin of the combined grid is located in the separation bubble where the wave packet is still showing linear behaviour ($x = 0.75$ m) and the grid extends to the end of the test section ($x = 2.0$ m). Only the UV -orientation of the cross-wire probe was used for this centreline plane.

In an effort to capture the three-dimensionality of the flow, data were measured on eight spanwise planes, normal to the test surface. Another spanwise plane consists of a uniform 10×10 mm grid at a fixed wall distance of $y = 10$ mm from the test surface consisting of $(N_x, N_z) = (126, 41)$, i.e. 5166 data points. The data for the spanwise planes contain U , V and W data requiring that the measurements be performed twice (once for the UV - and again for the UW -orientation of the cross-wire probe). Temporal mean velocity and broadband Reynolds stress measurements have also been measured without the disturbance. The same streamwise and horizontal grids were used while only five of the spanwise planes normal to the wall were used for the comparison.

The formation of vortex loops in the reattachment region is studied in detail using a true three-dimensional grid consisting of $(N_x, N_y, N_z) = (45, 17, 41)$ data points. The 31 365 grid points were also measured twice, using both orientations of the cross-wire probe, to obtain all three velocity components. The cross-wire measurements on the three-dimensional grid required a total of 31 days of continuous operation of the automated facility.

3. Undisturbed mean flow

The centreline pressure coefficient distributions for the laminar layer and the fully turbulent layer of Spalart & Watmuff (1993) are shown in figure 2. The major difference between the C_p distributions associated with the laminar and turbulent layers can be attributed to the presence of the separation bubble. Phase-averaged measurements are presented in §4, in which a small-amplitude impulsive disturbance is introduced at the C_p minimum at $x = 0.6$ m. The C_p distribution for this case is shown separately because the reattachment point on the centreline moves slightly upstream when the disturbance is introduced into the layer.

The flow can be divided into four distinct regions as labelled in figure 1. The first region, labelled [1], signifies where the laminar boundary layer develops in the FPG. Region [2] corresponds to the vicinity where the laminar layer separates in the APG leading to the formation of a detached shear layer. This region has been further subdivided into the two regions labelled [2a] and [2b], depending on whether the amplitude of the wave packet generated by the impulsive disturbance decays or amplifies with streamwise distance. Region [3] is characterized by the rapid growth of unsteadiness and the turbulent reattachment. Region [4] consists of the turbulent boundary layer downstream of the reattachment.

3.1. Boundary layer properties in the FPG

The test plate forms an extension to the lower surface of the wind tunnel contraction. This is an undesirable configuration since the origin and upstream history of the boundary layer at the entrance of the test section are unknown. However the FPG provides several beneficial effects, i.e. it presents a strong stabilizing influence and it improves the spanwise uniformity of the layer (see §3.4) and it is responsible for the development of a self-similar Falkner & Skan mean velocity profile.

The profiles near the entrance of the test section have inflection points close to the wall, which are presumably caused by the APG (which was not measured) near the exit of the contraction. These inflection points diminish with streamwise development and they are almost non-existent by $x = 0.4$ m. Towards the end of the FPG, there is a region of approximately 25 boundary layer thicknesses in length, where the free-stream velocity variation follows a power law, i.e. $U_1 \propto x^m$. The streamwise extent of the region ($0.42 \text{ m} < x < 0.55 \text{ m}$) was estimated by inspecting a log-log plot of U_1 versus x that was derived from interpolation of a cubic spline applied to the wall static pressure C_p data points shown in figure 2. The value $m = 0.28$ was obtained from a least-squares line of best fit over this streamwise range. In an effort to characterize the layer in this region, the profiles are fitted to the Falkner & Skan similarity solution using the wedge angle determined from the curve fit, i.e. $\beta = 2m/(m + 1) \approx 0.44$. The only adjustable constant is the effective origin for the layer, x_o , which corresponds to the minima of the sum of the squares of the deviations of the measurements from the Falkner & Skan profile.

Three experimental profiles are shown in figure 3(a) using the same effective origin, which is located 0.56 m upstream of the entrance to the test section, i.e. $x_o = -0.56$ m. The corresponding Falkner & Skan profile is shown together with the Blasius profile which is provided for reference. The experimental profiles match the Falkner & Skan profile reasonably well, with the possible exception of the profile at $x = 0.45$ m, which is the profile closest to the start of the region of constant β . The shape factors, $H = 2.34, 2.31$ and 2.34 , corresponding to profiles at $x = 0.45$ m, 0.50 m and 0.55 m, are in good agreement with the Falkner & Skan value of $H = 2.31$ for $\beta = 0.44$. The reasonably good fit of the experimental data suggests that the Falkner & Skan similarity solution would form a suitable inlet boundary condition for a numerical study of the separation bubble further downstream in the APG.

The momentum thicknesses of the three profiles in figure 3(a) are $\theta = 0.668, 0.651$ and 0.654 mm corresponding to the streamwise positions of $x = 0.45, 0.50$ and 0.55 m. The Reynolds numbers based on the momentum thickness and the local free-stream velocity are $R_\theta = 317, 318$ and 330 respectively. The corresponding Reynolds numbers based on the displacement thickness are $R_{\delta^*} = 742, 736$ and 774 respectively.

The Reynolds number towards the end of the FPG is approximately one order of magnitude less than the critical Reynolds number for the corresponding Falkner & Skan profile, see Obremski, Morkovin, & Landahl (1969). Therefore the FPG presents a very strong stabilizing influence and small-magnitude background disturbances of all frequencies originating from upstream sources are likely to decay to quite a small level before application of the APG.

3.2. Boundary layer separation in the APG

The free-stream velocity variation with streamwise distance also follows a power law in the APG, i.e. $\beta \approx -0.74$ in the region given by $0.66 \text{ m} < x < 0.70 \text{ m}$. This value of β is several times larger than the Falkner & Skan value corresponding to boundary layer separation (i.e. $\beta \approx -0.2$). Flying-hot-wire measurements (described in §3.3) have been used to estimate the streamwise location of the separation point on the centreline at $x = 0.64$ m, i.e. the layer separates before reaching this region of constant β . The centreline reattachment point is estimated from the flying-hot-wire data to be located at $x = 0.86$ m.

Mean velocity profiles obtained with the stationary normal hot-wire probe in the APG are plotted in three groups in figure 3(b–d). Profiles obtained near the end of the FPG are shown in figure 3(b) for reference purposes. The profiles in figure 3(b) that

are downstream of the separation (i.e. $x > 0.64$ m) clearly show the progression of the detached shear layer away from the wall. The reverse flow that occurs close to the wall cannot be determined with a stationary probe owing to hot wire directional ambiguity. Furthermore, rectification of the hot-wire signals will occur if the magnitude of the unsteadiness causes the velocity to change sign. Rectification will always introduce a positive error into the mean velocity measurements. The positive error owing to rectification will be largest when the mean flow is zero, which is one reason why the profiles do not contain points of zero velocity. Another explanation is that calibration of hot wires is notoriously difficult at low speeds. By repeating the stationary hot-wire measurements in the region of separated flow it was discovered that the most consistent data in the near-wall region are obtained if the zero velocity operating point is included in the calibration. Hot wires are extremely sensitive at zero velocity and small draughts in the test section can cause large voltage fluctuations. However there is evidence to suggest that flow reversals occur in this situation, i.e. the velocity time history contains points of exactly zero velocity where the hot-wire signals are subject to rectification. The operating point corresponding to zero velocity is taken to be the minimum voltage observed during a 30 s period after the wind tunnel fan becomes stationary. No attempt was made to account for the effects of natural convection in the hot-wire calibrations.

Profiles corresponding to the region labelled [2b] in figure 1 are shown in figure 3(c). These profiles coincide with the region of rapid growth of the disturbance-generated wave-packet amplitude with streamwise distance ($0.7 \text{ m} < x < 0.8 \text{ m}$). The continued progression of the detached shear layer away from the wall is clearly evident. The maximum shear in the mean flow, expressed as $\partial(\bar{U}/U_{\text{ref}})/\partial y$, decreases gradually in an almost linear manner over the range $0.72 \text{ m} < x < 0.78 \text{ m}$, which corresponds to the region where the maximum amplitude of the wave packet undergoes exponential growth with streamwise distance (see figure 9). The effects of hot-wire rectification, mentioned above, are also visible. The broadband unsteadiness level is of quite low magnitude in this region and the errors in the region of reversed flow remain fairly small. However, the broadband unsteadiness increases very rapidly for $x > 0.8 \text{ m}$ and the effects of hot-wire rectification become very pronounced near the wall, as shown in figure 3(d), especially in the vicinity of the mean reattachment point at $x = 0.86 \text{ m}$. The distributions of the mean shear and the broadband unsteadiness are shown in the contour plots in figure 5(b, c). The regions affected by hot-wire rectification errors, the relationship between the attributes of the separation bubble and the distributions of the mean shear and the broadband unsteadiness will be discussed in more detail in §3.3 below.

3.3. Flying-hot-wire investigation of the separation bubble

The flying-hot-wire technique involves propelling the probe in the upstream direction while measurements are made on the basis of the probe position. The superimposed bias velocity reduces the magnitude of the velocity fluctuations relative to the increased velocity experienced by the probe. Accurate measurements are possible in regions of reversed flow. As mentioned in §2.1, the maximum speed of the probe traverse in the x -direction is 1.5 m s^{-1} and this proved to be sufficient to overcome the small magnitude of the reversed flow in the separated region. The upstream velocity of the probe traverse is measured simultaneously with the hot-wire signal so that the velocity relative to a stationary observer can be obtained by subtracting this quantity from each probe measurement. Each upstream passage of the probe traverse results in a single sample at each position. Ensemble averages for the mean flow

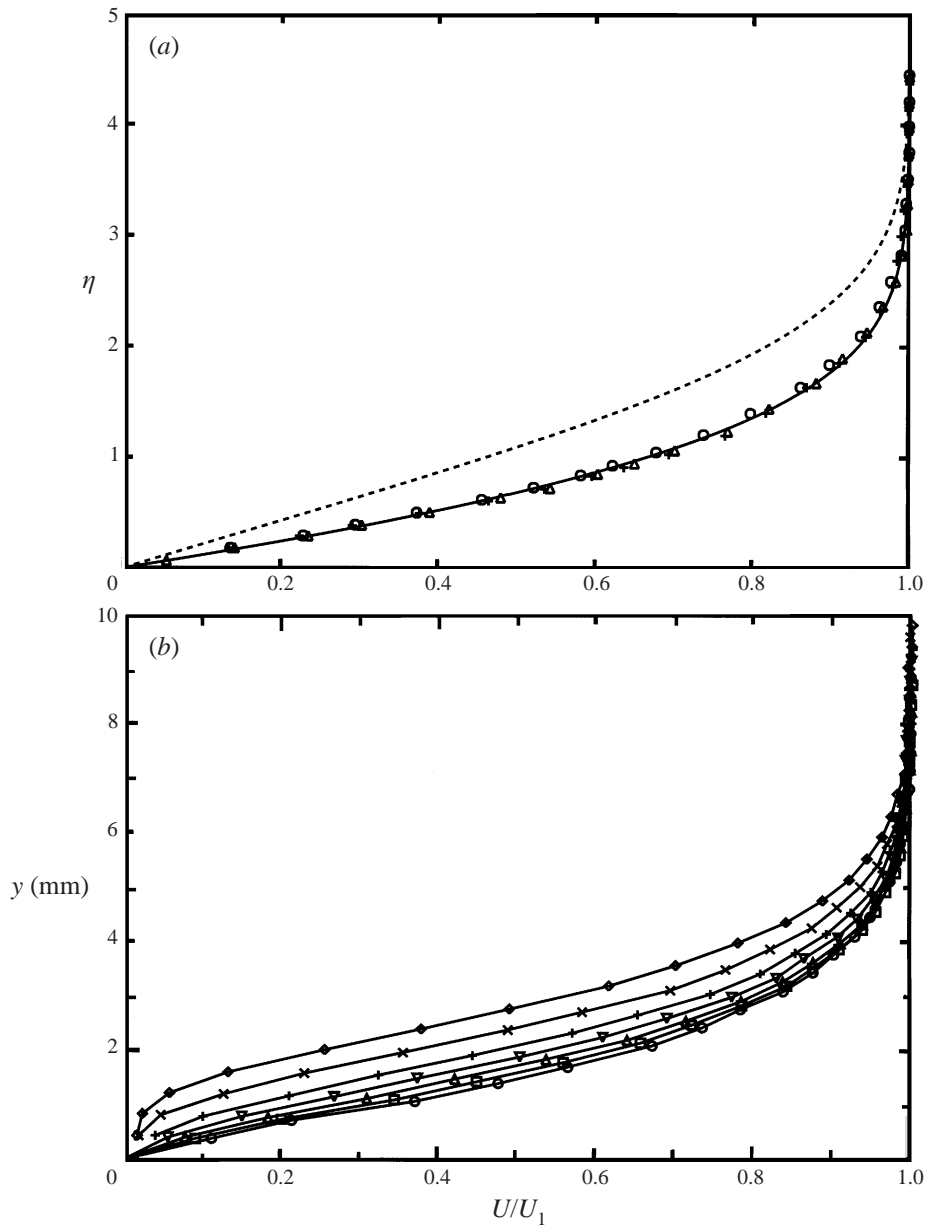


FIGURE 3 (a, b). For caption see facing page.

and Reynolds stresses are obtained by repeating the motion a sufficient number of times for statistical convergence of the ensemble-averaged data. Although it can be relatively time consuming to perform a large number of upstream traverse passes, one advantage of the technique is that the measurements are obtained in parallel for a large number of closely spaced data points.

The techniques for generating the sampling pulses that control the data acquisition and for deriving the analogue signal to represent the traverse speed follow the methods used by Watmuff *et al.* (1983). Briefly, the probe position and velocity are

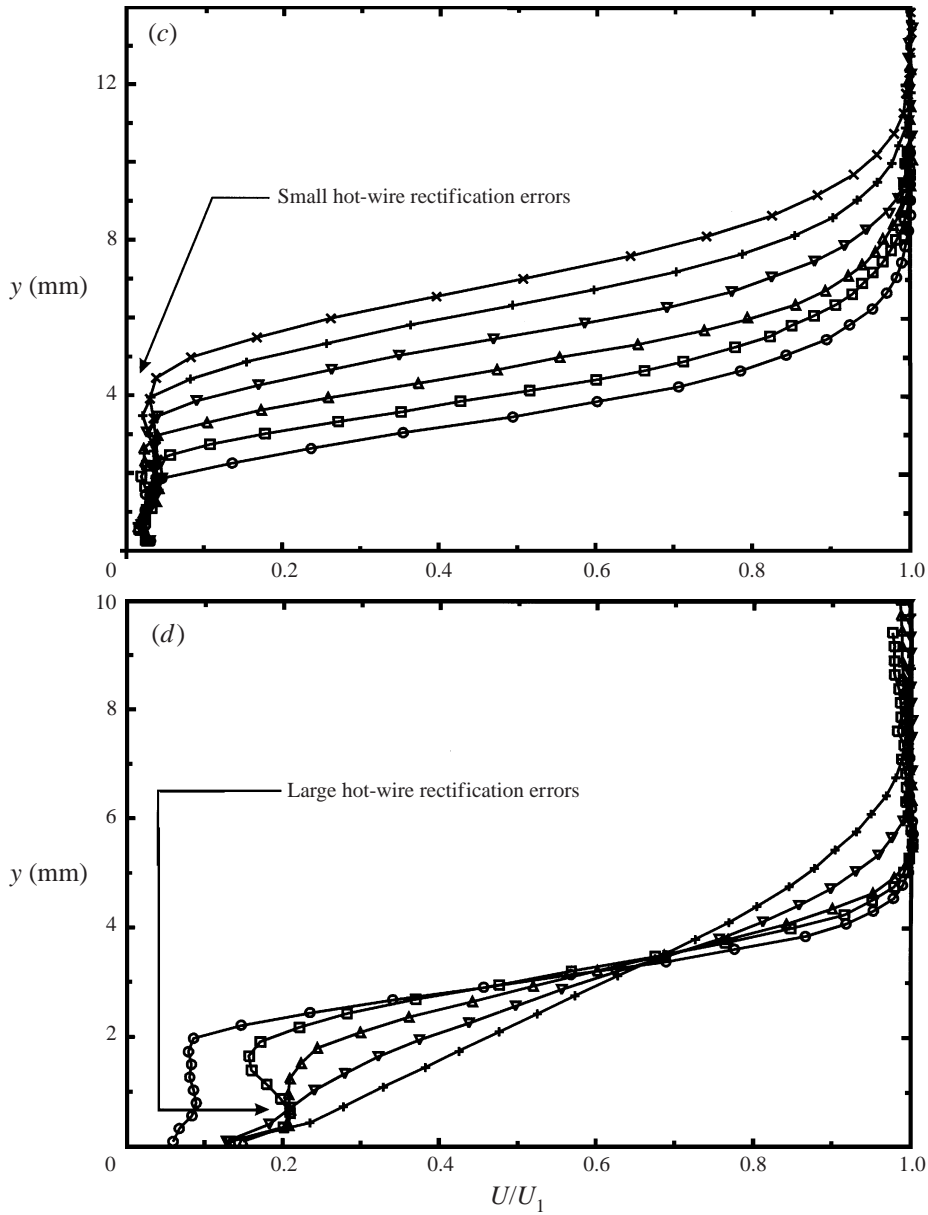


FIGURE 3. Centreline mean velocity profiles from a stationary hot-wire probe without the presence of the disturbance. (a) FPG profiles in Falkner & Skan coordinates: —, similarity solution using effective origin, $x_o = -0.56$ m and measured value, $\beta = 0.44$; ----, Blasius profile, $\beta = 0$; measurements at x positions, \circ 0.45; \triangle 0.50; $+$ 0.55 m. (b) APG region [2a], decay of wave packet amplitude: measurements at x positions, \circ 0.56; \square 0.58; \triangle 0.60; ∇ 0.62; $+$ 0.64; \times 0.66; \diamond 0.68 m. (c) APG region [2b], spanwise dispersion of waves and exponential growth of maximum wave packet amplitude: measurements at x positions, \circ 0.70; \square 0.72; \triangle 0.74; ∇ 0.76; $+$ 0.78; \times 0.80 m. (d) Reattachment region [3] and start of turbulent boundary layer, region [4]: measurements at x positions, \circ 0.82; \square 0.84; \triangle 0.86; ∇ 0.88; $+$ 0.90 m.

derived from an optical linear encoder with a resolution of $10\ \mu\text{m}$ and a maximum speed rating in excess of $2\ \text{m s}^{-1}$. Optical switches are used to detect the presence of the traverse at either end of the measurement trajectory. The signals from the two optical switches are combined in such a way as to produce a digital signal which indicates when the traverse is located between the two switches and when it is moving upstream. This signal is used to start the sampling. The signals from the encoder are combined digitally to produce a pulse train consisting of 100 pulses per mm of traverse movement. The pulse train is demodulated using a fourth-order Butterworth filter and amplified to produce a signal proportional to the traverse speed. The traverse-speed signal is calibrated by driving the input with a signal generator whose output is measured with an accurate digital frequency meter. For the present measurements, the traverse is accelerated from a position downstream of the first switch and the encoder pulse train is divided digitally by 100 to generate sample pulses at $\Delta x = 1\ \text{mm}$ intervals along the test section.

Unfortunately, the total time for a single measurement cycle is quite long, i.e. around 8 s. However, the primary objective for performing the flying-hot-wire measurements is to measure the reverse flow within the separated region. Since the flow in the separated region is relatively steady, only 500 upstream passes are required for adequate convergence of the mean flow. The mean velocity relative to a stationary observer, \bar{U} , and the mean square of the fluctuating component, $\overline{u^2}$, are shown in figure 4(a,b). The flying-hot-wire data are obtained at wall distances as close as $y = 0.5\ \text{mm}$. Point measurements of the deviations of the test-plate from the (x, z) -plane of the traverse have been made independently using a 10 mm square grid by attaching a dial gauge to the traverse. The deviations of the test plate over the entire traversable (x, z) -plane were found to be within $\pm 0.1\ \text{mm}$ which provides an estimate of the uncertainty of the wall distance.

A curious anomaly exists in the mean flow data for which a fully satisfactory explanation has not been found. Oscillations can be seen in the mean velocity distribution shown in figure 4(a) in the region given by $0.9 < x < 1.0\ \text{m}$, corresponding to the turbulent boundary layer just downstream of the reattachment. The oscillations could be the result of a standing wave pattern or other non-uniformity in the mean flow. This possibility was explored with a stationary cross-wire probe by measuring profiles normal to the test plate that were very closely spaced in the x -direction. However, no evidence of a standing wave pattern was found to exist. Another possibility is that the oscillations may be the result of probe vibration. However, it is unlikely that the phase of the vibrations would correlate so well with streamwise position, which is a necessary condition for the oscillations to appear in the ensemble averages. One hypothesis, suggested by a referee, is that the phase of the vortex shedding could be somehow triggered by the motion of the probe. The frequency ($f = 87\ \text{Hz}$) and wavelength ($\lambda_c \approx 0.05\ \text{m}$) of the waves provide an estimate of their propagation speed as $U_c \approx 4.35\ \text{m s}^{-1}$. The upstream speed of the probe for these measurements is given by $U_p \approx 1.2\ \text{m s}^{-1}$. Assuming that the wavelength of the fluctuations downstream of the reattachment is the same as that of the waves upstream, then the time interval corresponding to the wavelength of the fluctuations observed by the probe is given by $\Delta T = \lambda_c / (U_p + U_c) \approx 9\ \text{ms}$. The wavelength seen by the moving probe, λ_p , is given by the probe travel during this interval, i.e. $\lambda_p = 10.8\ \text{mm}$. This compares favourably with the wavelength of the oscillations seen in figure 4(a), i.e. $\lambda_p = 11.2\ \text{mm}$. A plausible mechanism by which the upstream motion of a probe could lock-in the phase of the vortex shedding process has not been identified and the correspondence between calculated and measured wavelengths

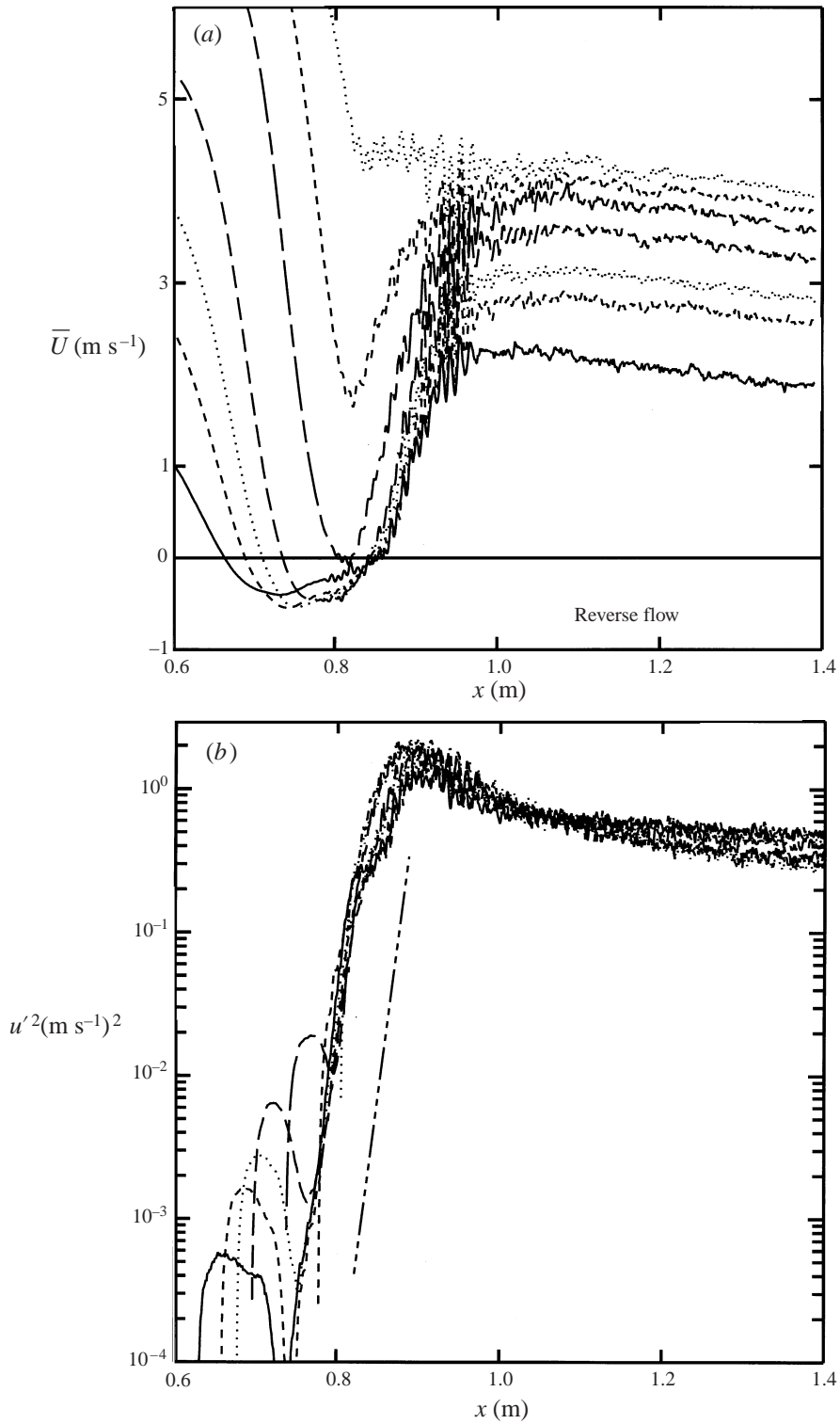


FIGURE 4. Flying-hot-wire measurements along streamwise trajectories on the centreline at various wall distances, without disturbance. (a) Mean streamwise velocity relative to a stationary observer. (b) Mean square of velocity fluctuations. Wall distances: —, 0.5; - - - -, 1.0; ·····, 1.5; — — —, 2.0; — — — —, 4.0; - - - - -, 6.0; ······, 8.0 mm. — — — — —, Average growth rate.

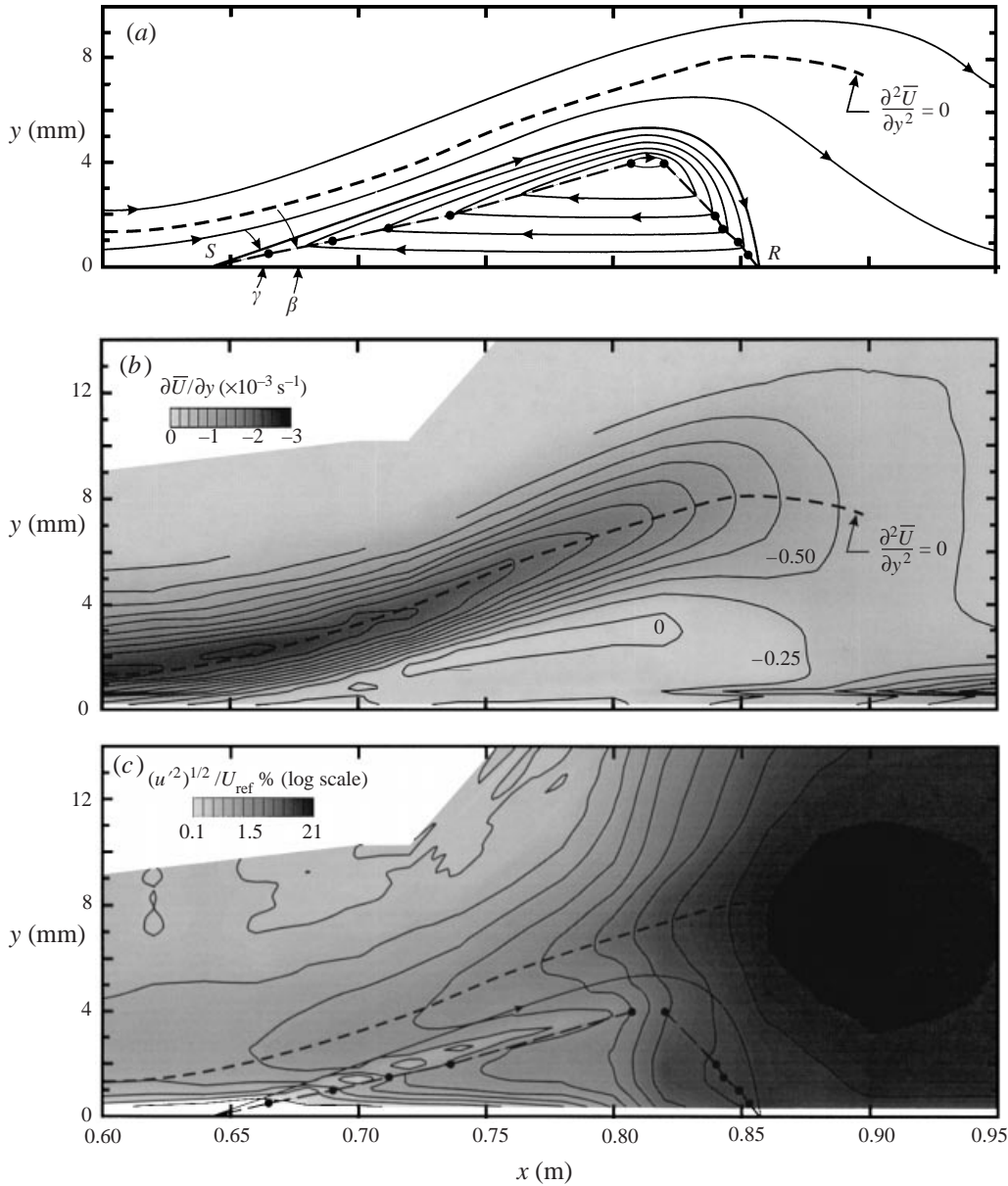


FIGURE 5. (a) Sketch of plausible temporal mean streamline pattern of the separation bubble deduced from flying-hot-wire measurements (\bullet , $\bar{U} = 0$, from figure 4a). Extrapolation to the wall to estimate the temporal mean centreline locations of separation, S at $x = 0.64$ and re-attachment, R at $x = 0.86$ m. Slope of isocline, $dy/dx = \infty$, defines β , and γ is the slope of the separation streamline. (b) Contours of $\partial \bar{U} / \partial y$ from normal hot-wire measurements with stationary probe. (c) Contours of background unsteadiness, $(\bar{u}^2)^{1/2} / U_{\text{ref}}$, with the outline of the bubble and isocline, $\bar{U} = 0$, superimposed. - - - -, $\partial^2 \bar{U} / \partial y^2 = 0$, from profiles (e.g. see figure 3), faired by hand and shown in all figures.

could be fortuitous. In any case, the triggering of the phase of the vortex shedding process does not appear to introduce serious error, as indicated by the good agreement between the stationary- and flying-hot-wire profiles in figure 6.

The distribution of the mean square of the fluctuating component, $\overline{u^2}$, appears

to pass through a local maximum and a local minimum before undergoing an approximately exponential growth rate in the region $0.75 \text{ m} < x < 0.85 \text{ m}$. The minima in $\overline{u^2}$ are consistent with the presence of a region of low background unsteadiness that is observed in data obtained with a stationary probe and will be further discussed below. The average growth rate of $\overline{u^2}$ is shown in figure 4(b) for comparison with the growth of the wave-packet amplitude in figure 9. While a larger number of samples would be required for improved convergence of $\overline{u^2}$, the convergence of \overline{U} is sufficient to determine the streamwise location of the point $\overline{U} = 0$ at each y -position with considerable certainty. Inspection of figure 4(a) shows that the region of reversed flow is confined within a wall distance of about 4 mm.

Direct examination of the mean velocity vectors has not been performed using a flying cross-wire probe. However it is possible to deduce a plausible representation of the temporal mean separation bubble from the normal hot-wire data by assuming a perfectly two-dimensional flow. For each of the five trajectories given by $y < 4 \text{ mm}$, the two streamwise positions where $\overline{U} = 0$ in figure 4(a) have been plotted in the (x, y) -plane shown in figure 5(a). These points are joined by dashed lines and they have been extrapolated to the wall to estimate the streamwise location of the separation point at $x = 0.64$ and the reattachment point at $x = 0.86 \text{ m}$. The region between the two dashed lines contains reversed flow and the tangent to the streamlines that cross each line must be in the y -direction (since $dy/dx = \infty$). This information acted as a guide for sketching the mean flow streamlines as seen by a stationary observer that are shown in figure 5(a).

It can be shown from critical point theory, e.g. Lighthill (1963), that the slope of the isocline given by $dy/dx = \infty$ is equal to $\frac{2}{3}$ of the slope of separation streamline defined by the angle γ given in (1.2). The measured value of $\tan \beta = 0.023$ (i.e. $\beta = 1.3^\circ$) and according to critical point theory the corresponding angle of separation should be $\gamma = 2.0^\circ$. The angles γ and β are shown in figure 5(a) and the slope of the separation streamline (based on the above considerations) provides additional information for sketching the mean flow pattern. The empirical relation for the angle of separation proposed by Dobbinga *et al.* (1972) is given by (1.3). The Reynolds number based on the free-stream velocity and momentum thickness at the separation point is $R_{\theta_s} = 387$. Therefore the angle between the test surface and the separation streamline predicted by the relationship of Dobbinga *et al.* is given by $2.2^\circ < \gamma < 2.9^\circ$. The relative difference between the measured and predicted estimates of the angle of separation is quite large but in absolute terms the difference is of order 0.5° and is considered to be acceptably small.

At the separation point on the centreline, $(1/\nu)(\partial \overline{U}/\partial \overline{x})_s = -0.16 \times 10^5 \text{ m}^{-2}$ and the momentum thickness, $\theta_s = 0.76 \text{ mm}$. Substitution into (1.1) leads to a value of the Thwaites (1949) pressure gradient parameter of $m = -0.092$. This compares favourably with the value of $m = -0.082$ suggested by Thwaites. Curle & Skan (1957) found $-0.171 < m < -0.068$ for the onset of separation. The value of the pressure gradient parameter m corresponding to separation in the present study is therefore consistent with prior experiments.

Gaster (1966) proposed that the condition for bursting of a short bubble is determined by a unique relationship between R_{θ_s} and a modified pressure gradient parameter, i.e. $(\theta_s^2/\nu) (\Delta U/\Delta x)$, where ΔU is the velocity difference based on the unseparated potential flow over the length of the bubble Δx . In the present study the quantities ΔU and Δx are estimated from the experimental turbulent boundary results of Spalart & Watmuff (1993) shown in figure 2. In terms of Gaster's nomenclature and classification, the separation bubble in the present study is considered to be a

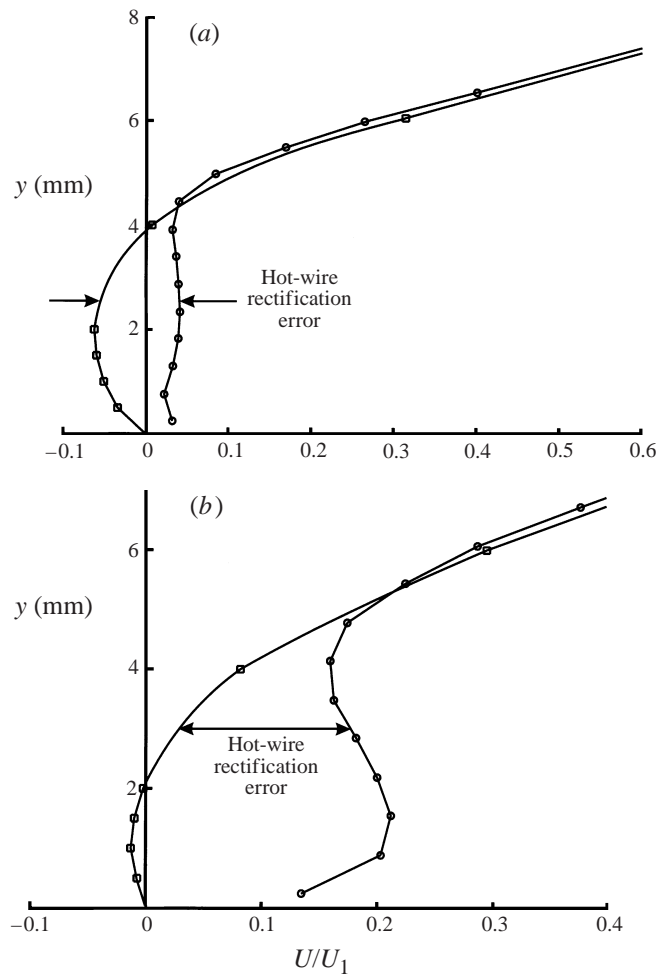


FIGURE 6. Comparison of inner region of mean velocity profiles measured with stationary and flying hot-wire probes, within the separation bubble and approaching reattachment. (a) $x = 0.80$ m, small fluctuation levels cause the region affected by hot-wire rectification errors to closely coincide with the region of reversed flow. (b) $x = 0.84$ m, larger fluctuations increase the relative size of the region affected by hot-wire rectification errors. \circ , Stationary probe; \square , flying hot-wire probe. Curves through sparse flying-hot-wire data faired by hand.

short bubble and the flow conditions are far from those corresponding to the onset of bursting to form a long bubble.

The relationship between the distribution of the mean shear, $\partial\bar{U}/\partial y$, and the characteristics of the separation bubble is not readily apparent from inspection of the profiles shown in figure 3(b-d). Contours of $\partial\bar{U}/\partial y$ derived from these normal hot-wire profiles (obtained with a stationary probe) have been plotted in the (x, y) -plane in figure 5(b) to readily allow a direct comparison to be made with features of the separation bubble. The quantity $\partial\bar{U}/\partial y$ represents the majority of the spanwise component of the vorticity since the quantity $\partial\bar{V}/\partial x$ is negligibly small. With the assumption of two-dimensional mean flow, the contours closely approximate the distribution of the temporal mean vorticity magnitude. The heavy dashed line shown in figure 5(b) has been faired by hand through the maxima of $\partial\bar{U}/\partial y(y)$ for each x -

position, i.e. the line represents the trajectory of the inflection points, $\partial \bar{U}^2 / \partial y^2 = 0$, in the mean velocity profiles. Comparison of figures 5(a) and 5(b) clearly shows that the region of maximum shear is located above the separatrix that defines the boundary of the bubble. In particular, it should be noted that the maximum shear is located well above the region of reverse flow. Contours of the r.m.s. unsteadiness arising from background disturbances are shown using a logarithmic scale for amplitude in figure 5(c). The trajectory traced out by the inflection points is also shown in the figure and it is evident that the trajectory coincides with the maxima in the background disturbance level at any given streamwise position. The observations provide strong evidence that the dominant instability mechanism is inviscid and associated with the inflectional velocity profiles.

It is interesting to note that a tongue-shaped region with an exceptionally low background unsteadiness level appears to coincide with the isocline $\bar{U} = 0$, just downstream of the separation. At first, the low levels in this region were thought to be anomalous and somehow associated with erroneous calibration of the hot wire at low velocities. However, further evidence for the validity of the data in this vicinity can be found in the flying-hot-wire measurements shown in figure 4(b). The trajectories at a constant wall distance clearly show a local minimum in $\overline{u'^2}$, which is consistent with the existence of the tongue-shaped region. It should be noted that the background unsteadiness level in this region is lower than that of the free stream.

Comparisons of the inner region of the mean velocity profiles obtained with a stationary and a flying hot-wire probe are shown in figure 6(a,b). The background unsteadiness is relatively small at $x = 0.80$ m and the region affected by hot-wire rectification errors coincides approximately with the region of reversed flow, as shown in figure 6(a). The extent of the region of temporal mean reverse flow diminishes as the reattachment is approached. However the relative size of the region affected by rectification errors becomes much larger because of the greater amplitude of the velocity fluctuations approaching the reattachment. For example, the profiles at the position $x = 0.84$ m, shown in figure 6(b), indicate that the region of reversed flow extends out to a wall distance of $y \approx 2$ mm, while the region affected by rectification errors extends to more than twice that wall distance, i.e. $y > 4$ mm. These comparisons between the stationary- and flying-hot-wire mean velocity profiles have acted as a guide for identifying regions in the phase-averaged data likely to be contaminated by hot-wire rectification errors. In particular, it should be noted that the wave packet measurements and the subsequent formation of vortex loops observed in §4 are mostly unaffected by hot-wire rectification errors.

3.4. Spanwise uniformity of the undisturbed mean flow

Observation of nominally two-dimensional laminar flows reveals an almost universal tendency to develop localized three-dimensional phenomena. Separated laminar flows are especially susceptible to this tendency. The three-dimensional phenomena can arise from the growth of initially small-amplitude instabilities that are excited by background environmental acoustical and vortical disturbances. An example of three-dimensional phenomena arising from local instability is considered in detail in §4. Additionally, localized three-dimensional phenomena can arise from small-amplitude mean-flow non-uniformities that are inherent in the upstream boundary layer.

The spanwise uniformity of the boundary layer is examined using velocity contours derived from the total pressure measured with a 1.54 mm diameter Pitot tube positioned flush with the test surface. The velocity is calculated using the static pressure on the centreline (corresponding to the streamwise position of the Pitot tube) that

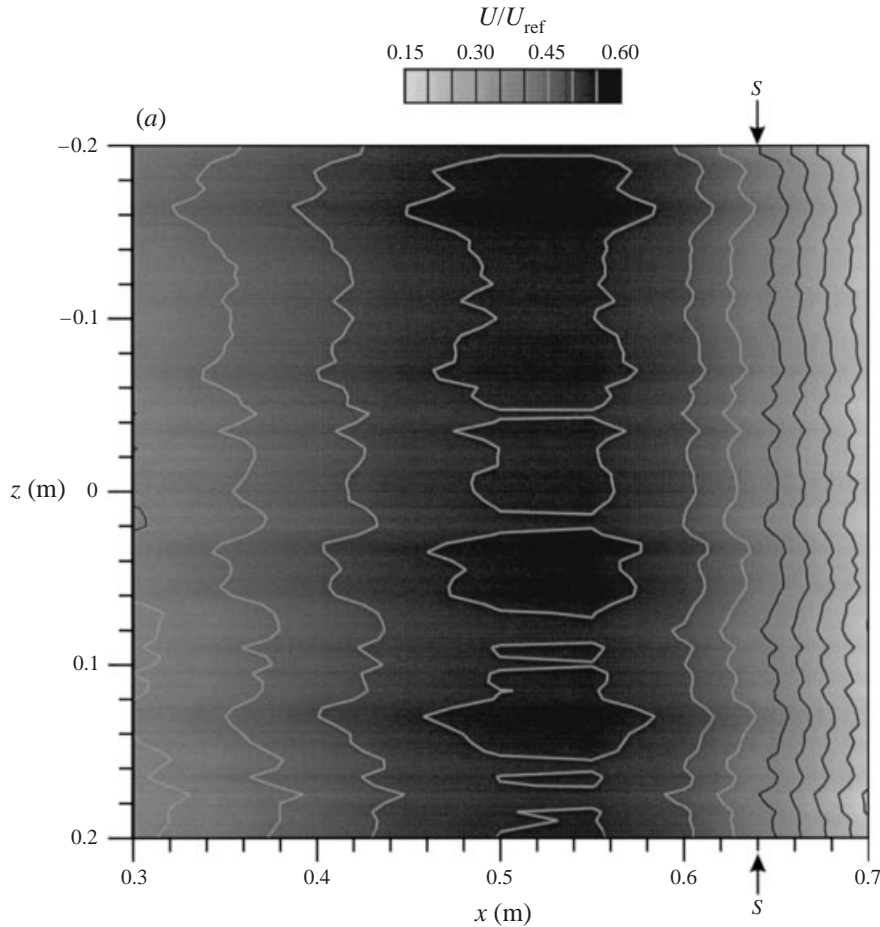


FIGURE 7 (a). For caption see facing page.

was obtained from a cubic spline applied to the centreline C_p measurements shown in figure 2. The grey-scale contour levels of velocity in figure 7(a) are obtained from measurements on a uniform rectangular grid consisting of $(N_x, N_z) = (9, 81)$, i.e. 729 data points, with spacing $\Delta x = 25$ and $\Delta z = 5$ mm. The effects of shear and other wall effects make it difficult to attach precise meaning to the data in general. However, in the FPG region, a considerable proportion of the mean velocity profile is approximately linear with wall distance, as shown in figure 3(a, b). The extent of the linear variation with wall distance exceeds the diameter of the Pitot tube. Therefore, at a given streamwise position in the FPG, the magnitude of the spanwise variations in velocity about the mean value also correspond to spanwise variations in the skin friction. The FPG has the beneficial effect of reducing the spanwise non-uniformity of the layer. For example, the spanwise variation of skin friction at $x = 0.3$ m is within $\pm 6\%$ while at the end of the FPG, at $x = 0.6$ m, the variation is within $\pm 2\frac{1}{2}\%$ of the mean value across the span.

Note the appearance of streamwise streaks that are associated with regions of locally higher velocity in the contours in figure 7(a). The origin of these streaks is unknown. The elevated levels suggest that the layer could be locally thinner in the vicinity of the streaks but this has not been confirmed by independent measurement.

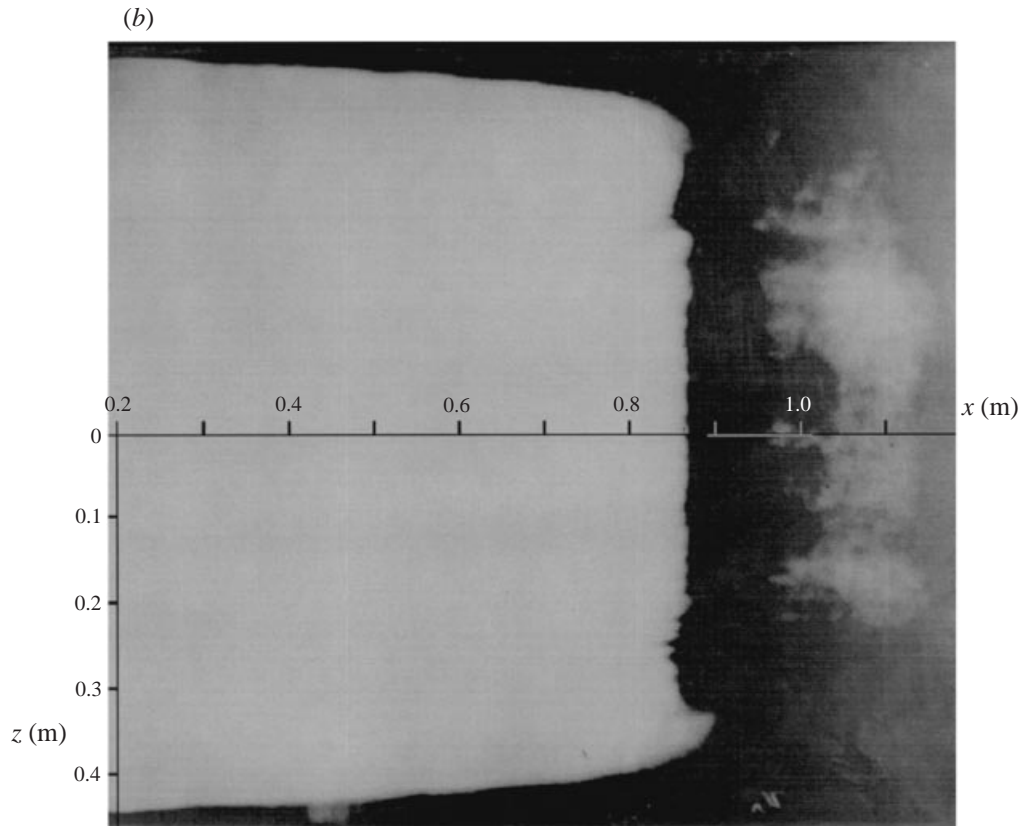


FIGURE 7. Undisturbed mean flow two-dimensionality. (a) Velocity inferred from a 1.54 mm diameter Pitot tube flush with the test surface. Arrows labelled *S* indicate centreline separation point. Grid details: $(N_x, N_z) = (9, 81)$, $\Delta x = 50$, $\Delta z = 5$ mm. (b) Photograph of naphthalene sublimation flow-visualization study.

The spacing of the streaks in the spanwise direction does not appear to be strongly correlated with length scales based on the boundary layer thickness. It is noted that these streaks persist in the contours after the layer has separated but it has not been determined at this stage whether they are associated with the spanwise variations in mean flow quantities observed in the vicinity of the reattachment (e.g. figure 8a).

A photograph of the result of a naphthalene sublimation flow visualization study is presented in figure 7(b). Higher magnitude skin friction associated with turbulent flow leads to more rapid sublimation and the photograph was acquired just after the naphthalene had been completely scoured from the test surface in the reattachment region. The streamwise location of the mean reattachment on the centreline (as indicated by the removal of the naphthalene) is in very good agreement with the location determined from the flying-hot-wire measurements (i.e. $x = 0.86$ m). The development of the turbulent corner flows associated with the sidewalls (i.e. $z = \pm 0.5$ m) are also clearly visible in the photograph. The contamination by the corner flows appears to be confined to the extremities of the test section and the overall two-dimensionality of the reattachment appears to be acceptable, at least on a large scale.

Spanwise variations exist on a finer scale within the reattachment region. The

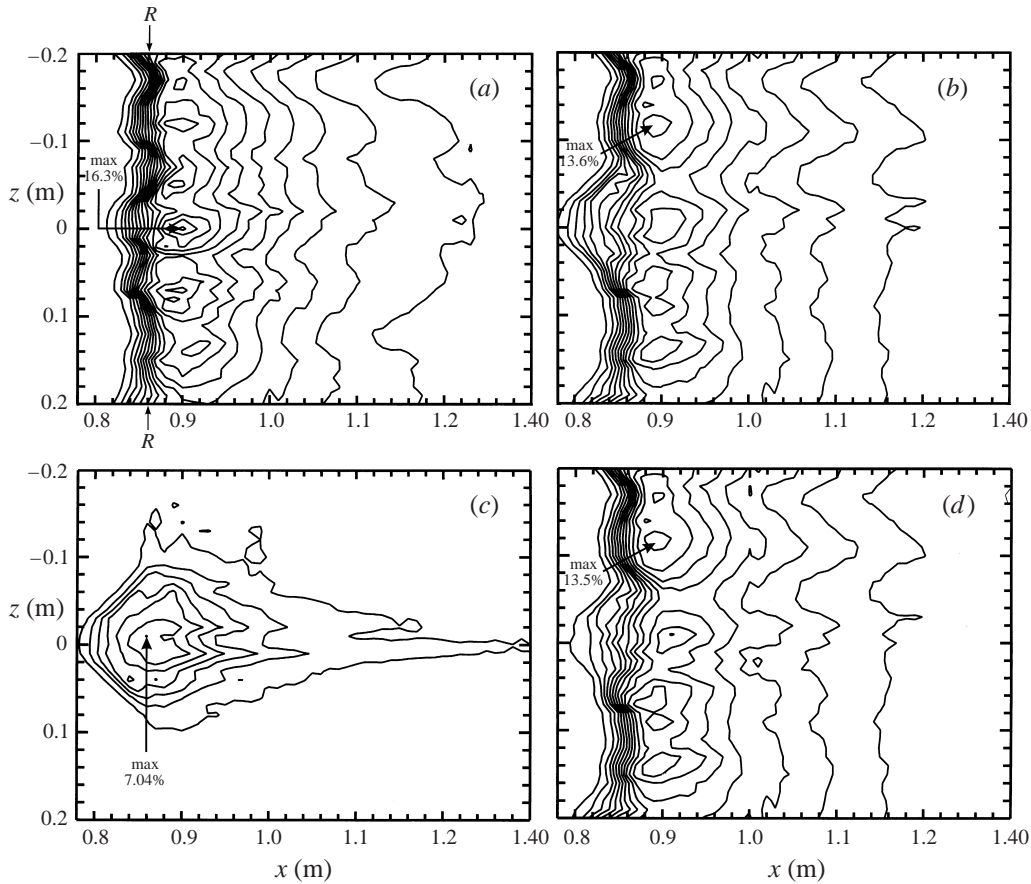


FIGURE 8. Components of r.m.s. velocity fluctuation normal to the test surface in plane $y = 10$ mm. Broadband component, $(\overline{v'^2})^{1/2}/U_{\text{ref}}$ (a) without disturbance (arrows labelled R indicate centreline reattachment point), and (b) with disturbance. Phase-averaged components (i.e. with disturbance), (c) contribution, $(\overline{v'^2})^{1/2}/U_{\text{ref}}$, and (d) background, $(\overline{v'^2})^{1/2}/U_{\text{ref}}$. Grid details: $(N_x, N_z) = (63, 41)$, i.e. 2583 data points, $\Delta x = \Delta z = 10$ mm. CI = 1.0% (CI is contour increment).

variation in the mean velocity was found to be less pronounced than the variations in the r.m.s. of the fluctuating quantities which are briefly considered here. Contours of the velocity fluctuations normal to the wall are shown in figure 8(a-d). The contours are derived from cross-wire data, obtained on the uniform rectangular measurement grid that is aligned parallel to the test surface at $y = 10$ mm. The evolution of an impulsive disturbance deliberately introduced at the C_p minimum is considered in §4. The broadband distribution $(\overline{v'^2})^{1/2}/U_{\text{ref}}$, is shown without the impulsive disturbance in figure 8(a), and with the disturbance acting in figure 8(b). The reduction in the peak amplitude when the disturbance is present, as shown in figure 8(b), and the contours of phase-averaged quantities in figure 8(c, d) will be discussed in §4.

One manifestation of the spanwise non-uniformity in figure 8(a) is the waviness of the contours upstream of the reattachment. Another manifestation is the spanwise variations in the peak values which are located about 40 mm downstream of the centreline reattachment point, which is indicated by the arrows labelled R in figure 8(a). It is clear that the spanwise location of the peak amplitude levels downstream of the reattachment correlate well with corresponding regions of elevated amplitude at

positions upstream of the reattachment. This apparently self-evident observation does not hold for the case when the impulsive disturbance is deliberately introduced in the layer, as shown in figure 8(b). In fact, the peak r.m.s. amplitudes in the vicinity of the centreline are smaller when the disturbance is present in the layer.

The spanwise variations of the peak amplitude in the vicinity of $x = 0.9$ m in figure 8(a) are greater than $\pm 25\%$ of the mean value across the span. It is unclear whether the clustering of the peak values is associated with (a) nonlinear growth of instabilities originating upstream, (b) small-amplitude non-uniformities inherent in the layer, or (c) another, as yet unknown cause. However, it is plausible that the phenomena responsible for the clustering of the contours could be related those responsible for the three-dimensional cellular features observed in the oil-flow pattern in the reattachment region behind a backward facing step, as observed by Roshko & Thomke (1966) and in the oil-flow pattern for the hemisphere-cylinder at zero angle of attack shown by Peake & Tobak (1980).

4. Phase-averaged measurements

As mentioned previously, a small-amplitude impulsive disturbance is introduced repetitively through a 0.6 mm diameter hole in the test surface at the C_p minimum, as shown schematically in figure 1. The evolution of the disturbance is tracked from its source, all the way into the reattachment region and beyond into the fully turbulent boundary layer.

4.1. Formation and development of the wave packet

Phase-averaged normal hot-wire data have been measured on 42 spanwise (y, z)-planes spaced at $\Delta x = 10$ mm intervals along the test section using a stationary probe. Each (y, z)-plane consists of $(N_y, N_z) = (17, 11)$, i.e. 187 data points. The first spanwise plane is located 10 mm upstream of the hole at the C_p minimum where the disturbance is introduced and the last plane is located 0.14 m downstream of the reattachment, i.e. at $x = 1.0$ m. Directly above the hole, at the C_p minimum, the disturbance penetrates only about 1 mm into the layer and it has a maximum negative amplitude of $0.03U_{\text{ref}}$.

One way of characterizing the growth of the disturbance is to consider the variation of the phase-averaged amplitude with streamwise distance. The maximum r.m.s. amplitude of the phase-averaged perturbations, considering all points in each spanwise plane, is plotted against streamwise distance in figure 9. In terms of the definitions given in §2.3, the notation for the r.m.s. amplitude is $u_\phi = (\bar{u}^2)^{1/2}$. At first, the layer is attached and the maximum r.m.s. amplitude decays exponentially with streamwise distance. The rate of decay is reduced after the layer separates, at $x = 0.64$ m, and the maximum r.m.s. amplitude observed in the spanwise planes reaches a minimum value, $u_\phi(y, z) = 0.0018U_{\text{ref}}$, at $x = 0.68$ m. From this point the amplitude increases and ultimately undergoes exponential growth in the region given by $0.72 \text{ m} < x < 0.80 \text{ m}$. The average growth rate of the background disturbances (scaled from figure 4b) is shown in figure 9 and it is evident that the exponential growth rate of the wave packet is essentially the same as the background disturbances. Exponential variation of disturbance amplitude with Reynolds number is a characteristic often seen in the results of linear stability calculations. For example, Mack (1984) demonstrated exponential growth of the Tollmien–Schlichting wave amplitude with Reynolds number in the Blasius boundary layer over a substantial portion of the amplification range. Dovgal & Kozlov (1990) observed extensive regions of exponential growth with streamwise distance for two-dimensional waves in the separation bubble behind a hump on a flat

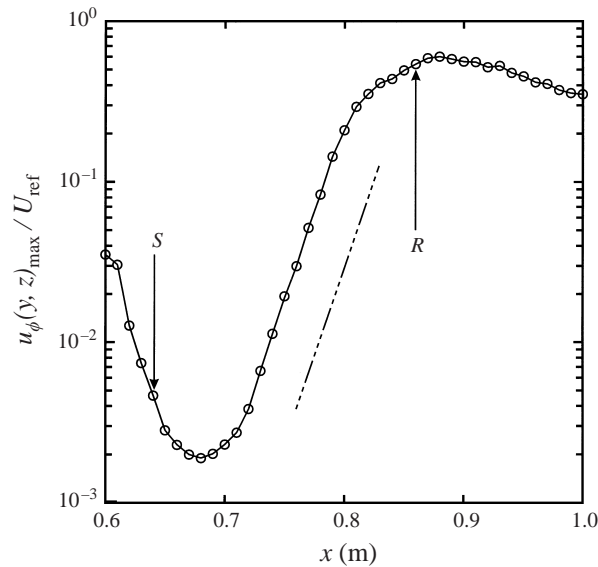


FIGURE 9. Development of the maximum r.m.s. amplitude of phase-averaged streamwise velocity perturbation in each of a number of (y, z) -planes. Arrows labelled S and R indicate the separation and reattachment points on the centreline without disturbance. ---, Average growth of background disturbances (from figure 4*b*).

test surface. They found that the growth rate of disturbances did not depend on the initial amplitude, when it is small enough, thereby indicating linear behaviour. Dovgal *et al.* (1994) note that 'linearity of disturbances with amplitude ... is a remarkable feature of separation bubbles'. The exponential growth of the wave packet amplitude shown in figure 9 suggests that the behaviour of the wave packet is linear, despite reaching the rather large amplitude of $u_\phi(y, z)_{\max} / U_{\text{ref}} \approx 20\%$ by the end of this region, at $x = 0.8$ m.

The streamwise development of the 99% boundary layer thickness is shown in figure 1. The layer thickness is derived from the closely spaced normal hot-wire profiles on the centreline and the development is correctly scaled with the test section geometry. On this scale, the growth appears to be almost linear up to the end of the region of exponential growth rate of the disturbance, given by $x = 0.8$ m. It is evident that the demise of linear behaviour in the disturbance growth rate coincides with the beginning of a region of rapid growth of the boundary layer thickness.

Waveforms of the phase-averaged perturbations are shown for all y -positions on the centreline for a number of streamwise planes in figure 10(*a-c*). The small-amplitude oscillations that are superimposed on the positive overshoot following the main large negative perturbation in figure 10(*a*) could be the result of transient acoustic reflections in the system used to introduce the disturbance. In any case, these oscillations decay with streamwise distance and they are only barely discernible at the temporal mean separation point, as shown in figure 10(*b*). The waveforms at all streamwise positions leading up to the separation point have much the same form. However, just downstream of the separation, a new small-amplitude positive perturbation emerges which is located ahead of the original negative component. The magnitude of the new positive perturbation grows with streamwise distance and by the streamwise position of minimum r.m.s. wave amplitude ($x = 0.68$ m), it is

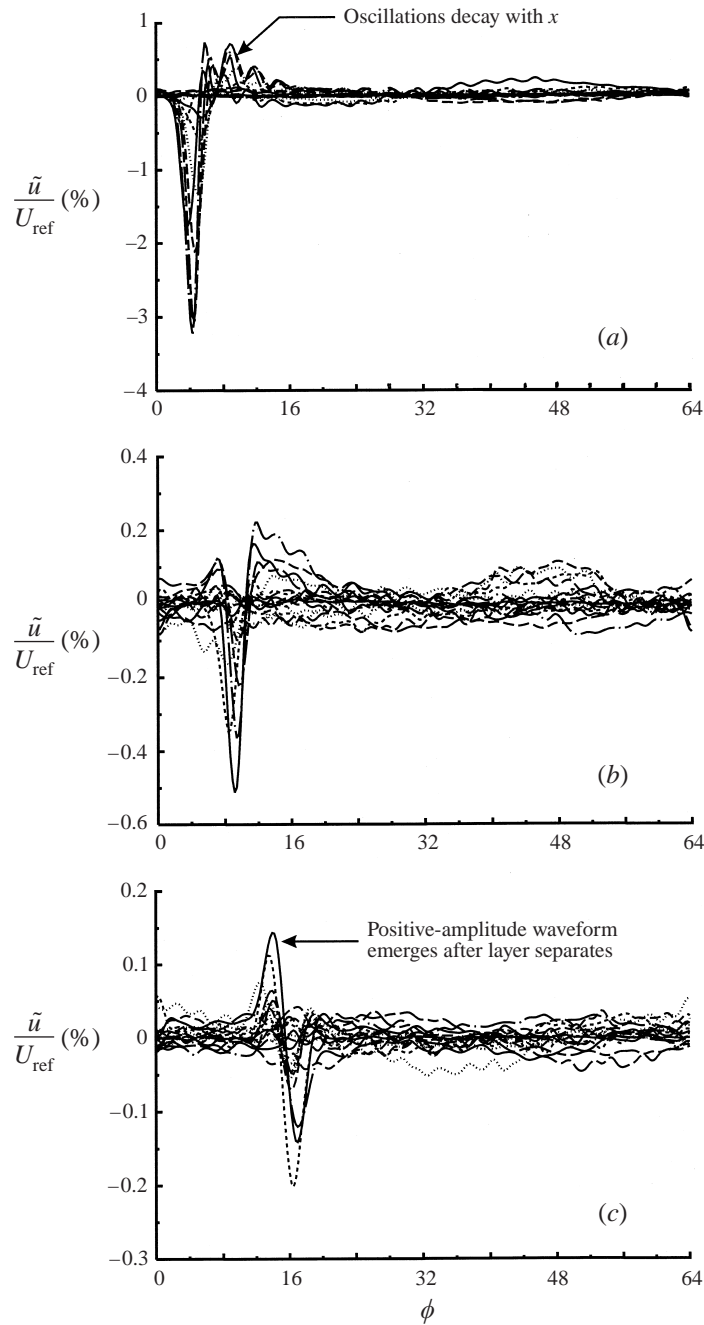


FIGURE 10. Phase-averaged streamwise velocity perturbation waveforms for all points ($N_y = 17$) on the centreline of the spanwise plane located at streamwise positions: (a) 10 mm downstream of source, $x = 0.61$ m, (b) temporal mean separation point, $x = 0.64$ m, and (c) streamwise position of minimum amplitude, $x = 0.68$ m.

approximately equal to the magnitude of the original negative perturbation, as shown in figure 10(c).

The spatial resolution of the phase-averaged data in the streamwise direction (i.e. $\Delta x = 10$ mm) is not sufficient to generate the true spatial contours of the disturbance

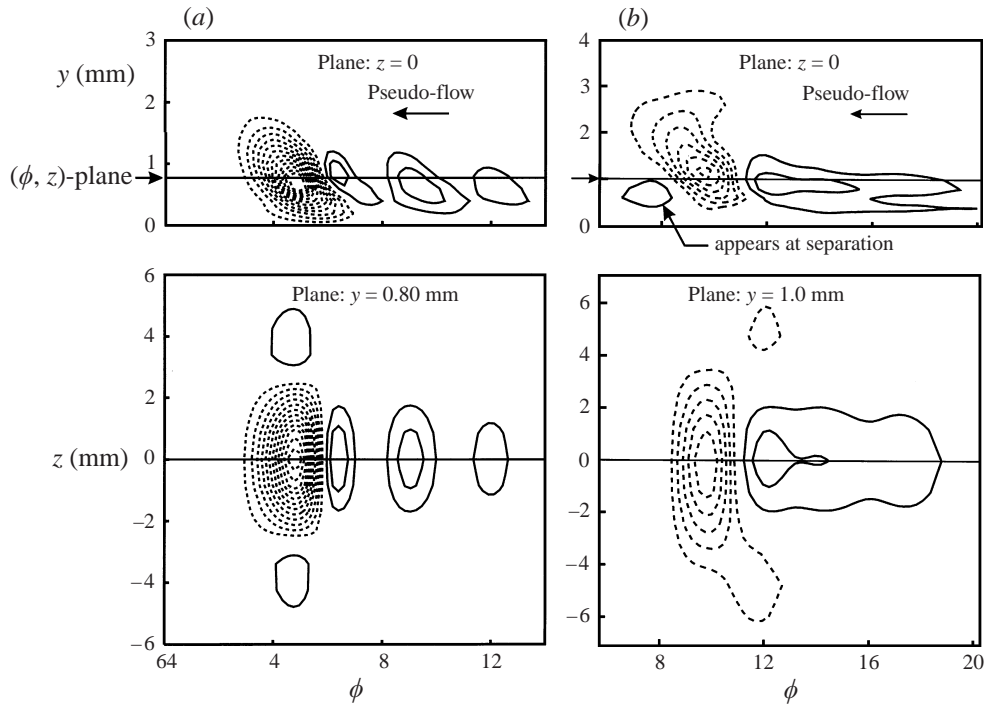


FIGURE 11. Development of contours of phase-averaged perturbation, \bar{u}/U_{ref} , in the attached layer. Phase, ϕ , applied as third coordinate to data in the (y, z) -plane (pseudo-flow visualization). (a) $x = 0.61$ m, CI = 0.25%, (b) $x = 0.64$ m, CI = 0.08%. Solid lines are positive and dashed lines are negative levels.

amplitude of the wave packet in detail. However, it should be noted that even if the streamwise spacing of the spanwise planes was reduced, it would still be difficult to present the true spatial three-dimensional contours of the disturbance amplitude associated with the wave packet, because of the exponential growth of the amplitude with streamwise distance. For example, the maximum r.m.s. amplitude varies by two orders of magnitude in the region given by $0.72 \text{ m} < x < 0.80 \text{ m}$. In this vicinity a lack of convergence or scatter in the phase-averaged waveforms of only a few percent in one region of a contour plot could correspond to a large percentage of the entire perturbation in a nearby region.

By using phase, ϕ , as the third streamwise coordinate, it is possible to construct a three-dimensional representation of the disturbance from the data in each spanwise plane. A series of contour plots have been made in the (ϕ, y) - and (ϕ, z) -planes, as shown in figure 11, figure 12 and figure 13. This technique will be referred to as pseudo-flow visualization. The contours of the wave-packet amplitude have been generated from cubic spline interpolation of the phase-averaged data onto a uniform three-dimensional grid in (ϕ, y, z) space. The purpose of the interpolation is to obtain a higher degree of smoothness for the contours and it should be emphasized that the splines pass through all the measured data points. The pseudo-flow field will only provide an accurate reproduction of the true (spatial) flow field if all disturbances are propagating at an approximately constant streamwise velocity and the streamwise derivatives of quantities are small, e.g. Taylor's hypothesis in turbulent flow. Neither

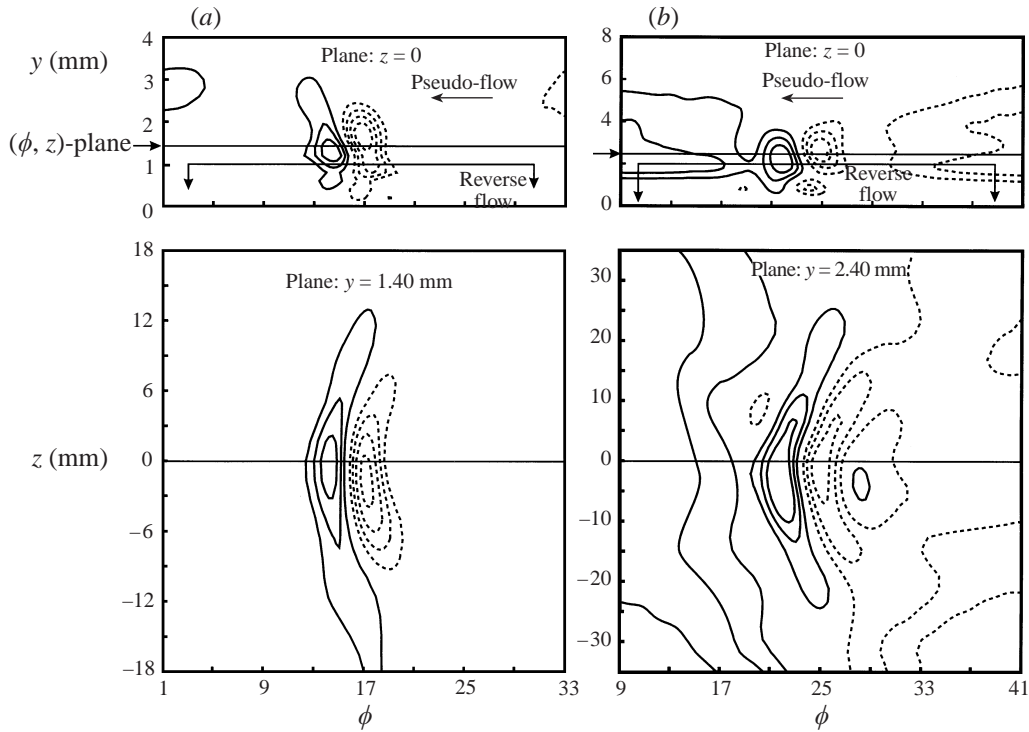


FIGURE 12. Pseudo-flow visualization contours of \tilde{u}/U_{ref} showing the development of dispersive wave characteristics in separated layer. (a) Position of minimum r.m.s. wave amplitude, $x = 0.68$ m, $\text{CI} = 0.04\%$. (b) Start of region with exponential growth rate of r.m.s. disturbance amplitude with streamwise distance, $x = 0.72$ m, $\text{CI} = 0.10\%$.

of these assumptions is true in the APG and the interpretation of these contours must be made with some caution.

The overall shape of the perturbation remains much the same in the region where the layer is attached, as shown in figure 11(a, b). The non-dispersive characteristic of the contours and the exponential decay of the disturbance with streamwise distance are consistent with the notion that the flow in the APG is stable with respect to small disturbances while it remains attached. The counterpart of the small-amplitude oscillations, referred to previously in figure 10(a), appear as three waves with small positive amplitudes in figure 11(a). These waves appear to merge together with further streamwise development as shown in figure 11(b).

As noted previously, after the layer separates, the rate of decay of the disturbance with streamwise distance is reduced and a point of minimum amplitude is reached at $x = 0.68$ m (see figure 9). The pseudo-flow visualization contours of the disturbance amplitude corresponding to this position are shown in figure 12(a). By this streamwise position, a positive amplitude wave has emerged upstream of the original negative amplitude disturbance that was introduced at the hole. The spanwise extent of the negative wave has more than doubled, increasing from $\Delta z \approx 18$ mm, within a streamwise distance of $\Delta x \approx 40$ mm, which indicates the onset of considerable dispersion. With further streamwise development of $\Delta x \approx 40$ mm, the dispersion of the wave packet is clearly evident in the pseudo-flow visualization contours shown in figure 12(b). This position, i.e. $x = 0.72$ m, corresponds to the beginning of the region

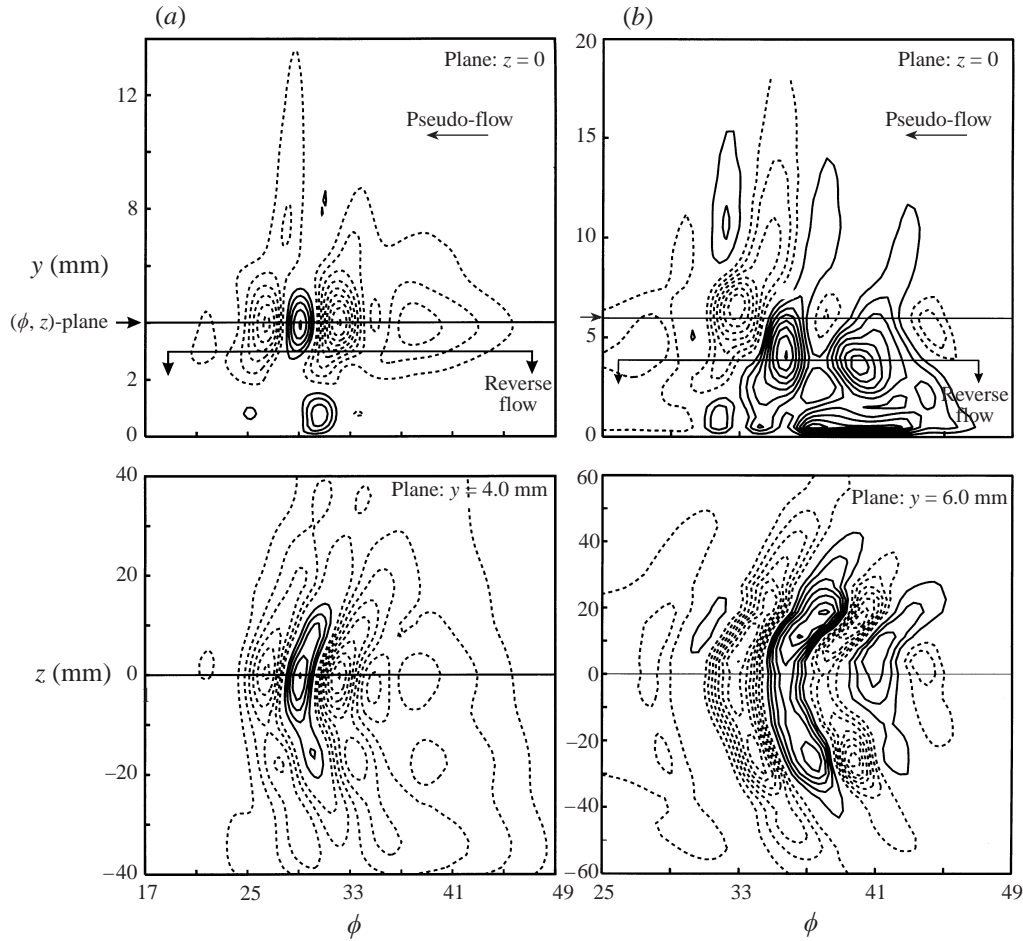


FIGURE 13. Pseudo-flow visualization contours of waves in the region of exponential growth rate of r.m.s. disturbance amplitude with streamwise distance: (a) $x = 0.76$ m, $CI = 0.5\%$, (b) $x = 0.80$ m, $CI = 2.5\%$.

of exponential growth of the maximum r.m.s. wave amplitude. Note that the region affected by the disturbance extends beyond the immediate vicinity of the wave packet in both the streamwise and spanwise directions at this location. A similar observation is reported in the review papers of Kozlov (1984) and Dovgal *et al.* (1986). They refer to experiments concerning the behaviour of a wave packet generated by a point source located upstream of a laminar separation bubble on the smooth surface of a wing. Considerable distortion of the flow in the bubble was also observed in these experiments in regions away from the immediate vicinity of the ensuing wave packet.

Pseudo-flow visualization contours of the wave packet in the region where the amplitude grows exponentially with streamwise distance are shown in figure 13(a,b). This region is characterized by an increase in the number of waves within the packet and considerable dispersion. As mentioned previously, the exponential growth suggests linear behaviour (in terms of linear stability theory) despite the rather large amplitudes of the disturbance, i.e. $\tilde{u}_{\max}/U_{\text{ref}} \approx 20\%$.

The local regions of maximum amplitude follow a trajectory corresponding to the inflection points in the mean flow. This suggests that the dominant instability

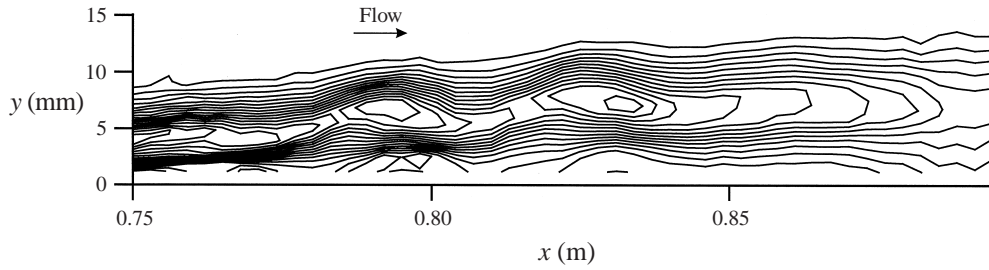


FIGURE 14. True (i.e. spatial) flow visualization contours of phase-averaged spanwise vorticity for Phase 31 calculated from cross-wire data on the centreline plane. The wave packet in figure 13 is associated with formation of Kelvin–Helmholtz cat’s-eyes in the detached shear layer. $CI = 100 \text{ s}^{-1}$.

mechanism governing the growth of the wave packet is inviscid. Further support for this assertion can be found in the true spatial flow visualization contours of the phase-averaged spanwise vorticity obtained in this vicinity that are shown in figure 14. The contours have been calculated from cross-wire data in the centreline plane. Comparison of figure 14 with figure 13(b) shows that the wave packet is associated with the formation of the cat’s eye pattern which is a characteristic of Kelvin–Helmholtz instability. Referring to figure 6(b), it should be noted that the cat’s eye pattern in figure 14 is located above the region affected by hot-wire rectification errors.

The perturbations in the spanwise vorticity in figure 14 are similar to those occurring in a free shear layer, i.e. the presence of the wall appears to exert little influence on the detached shear layer, at least during the initial stages. This observation suggests that the dominant wave frequency might be predicted from inviscid linear stability theory. For a free shear layer between two streams with velocity U_1 and U_2 , the velocity difference across the shear layer is given by $\Delta U = U_2 - U_1$ and the average velocity can be defined as $U_m = (U_1 + U_2)/2$. The vorticity thickness, $\delta_\omega = \Delta U / (\partial u / \partial y)_{\max}$ and the velocity ratio $\lambda = \Delta U / (2U_m)$ can be used to characterize the shear layer. Following Monkewitz & Huerre (1982) and Michalke (1964), the most amplified frequency may be expressed non-dimensionally as $\omega^* = \frac{1}{4} \delta_\omega 2\pi f / U_m$. The frequency of the most amplified mode predicted from inviscid linear stability theory for a parallel shear flow with a tanh velocity profile is given by $\omega^* = 0.21$.

Villiermaux (1998) investigated the effects of viscosity on the mode selection and associated growth rate in the inflectional instability of shear layers. A viscous correction term was derived for the most unstable mode and its growth rate in the form of a correction factor, i.e. $\{1 + [(a/0.2)/Re]^2\}$. The constant, a , is dependent on the shape of the initial velocity profile, e.g. $a = 1.216$ for the tanh profile, while $a = 3$ for the piecewise linear profile. The Reynolds number in the correction factor is based on half the velocity difference across the layer, $\Delta U/2$ and the vorticity thickness is used for the length scale. For the detached shear layer in the present investigation the viscous correction term of Villiermaux amounts to about 1 part in 10^4 , which is negligibly small. However, the mean flow is non-parallel and consideration of the stability characteristics is complicated by the presence of the APG. Nevertheless, the non-dimensional frequency, ω^* , predicted from inviscid linear stability theory is not strongly dependent on either λ or the profile shape for the case of parallel flow in a zero pressure gradient (ZPG). Therefore this parameter could still have some relevance in the present configuration, despite the rapid development with streamwise distance and the influence of the APG.

In contrast with a free shear layer in a ZPG, the free-stream velocity at the edge of the separated layer is ill-defined, i.e. $\bar{U}(y)$ does not tend to a constant as $y \rightarrow \infty$. The uncertainty is most pronounced in the vicinity of the reattachment. Owing to this uncertainty the following method is used to calculate ω^* . The maximum velocity in each profile is used to define U_1 . The flying-hot-wire data are used to estimate U_2 . The velocity gradient $(\partial u / \partial y)_{\max}$ is estimated numerically after visually identifying the region of linear variation in the profiles shown in figure 3(c). The frequency f is obtained from a well-defined, very narrow band of elevated energy level in the corresponding power spectra measurements obtained without the disturbance. The frequency f also closely corresponds to the passing frequency of the waveforms generated by the disturbance which has been estimated from the wavelength and propagation velocity of the wave packet. An approximately linear variation of ω^* with streamwise distance exists in the region of exponential growth, i.e. $\omega^* = 0.10$, $x = 0.70$ m $\rightarrow \omega^* = 0.25$, $x = 0.84$ m. Simple interpolation of a least-squares line of best fit applied to the data demonstrates that the inviscid linear stability theory value of $\omega^* = 0.21$ corresponds to the position $x = 0.80$ m. This is the location where the cat's eye patterns can be seen in the contours of the phase-averaged spanwise vorticity in figure 14. The observation is therefore consistent with the notion that an inviscid instability mechanism is responsible for the growth of the disturbance.

4.2. Formation of vortex loops in the reattachment region

A sequence from an animation of the spanwise vorticity contours derived from the cross-wire data measured in the centreline plane is shown in figure 15. The sequence is plotted using an increment of four phase intervals between each frame and the streamwise distance between the measurement grid points is $\Delta x = 3$ mm and 17 uniformly spaced grid points are used normal to the test surface. The concentration of spanwise vorticity in the form of the cat's eye patterns in the initial stages is reminiscent of the roll-ups that appear in a free shear layer. Four distinct regions of concentrated spanwise vorticity emerge in the vicinity of the reattachment. These regions are labelled A, B, C and D and a dashed line has been faired by hand between each one in the subsequent frames as a means of following their streamwise development. The first region, labelled A, appears to be short-lived, while the second region of concentrated spanwise vorticity, labelled B, accelerates away from the wall to become the dominant member of the group.

This vicinity of the flow field has been mapped out in great detail with a cross-wire probe using a true three-dimensional measurement grid of dimension $(N_x, N_y, N_z) = (45, 17, 41)$. The 31 365 data points were measured twice, using both orientations of the cross-wire probe, to obtain all three velocity components. These measurements required a total of 31 days of continuous operation of the automated facility. A sequence taken from an animation of a contour surface of vorticity magnitude is shown in figure 16. The vorticity magnitude level used for the contour surface is given by $|\Omega| = 140$ s⁻¹, which was calculated from the quantities $\langle U \rangle$, $\langle V \rangle$ and $\langle W \rangle$. The data have not been interpolated and smoothing has not been applied to the phase-averaged velocities to reduce the scatter introduced by the differentiation required for calculation of the vorticity magnitude. The evolution of the three-dimensional waves into a group of large-scale vortex loops is clearly visible. It is evident that the regions of concentrated spanwise vorticity that appear in the centreline plane in figure 15 correspond to sections through three-dimensional roll-ups that evolve into vortex loops.

At first (e.g. Phase 35 in figure 16), the roll-ups are only slightly bowed and the

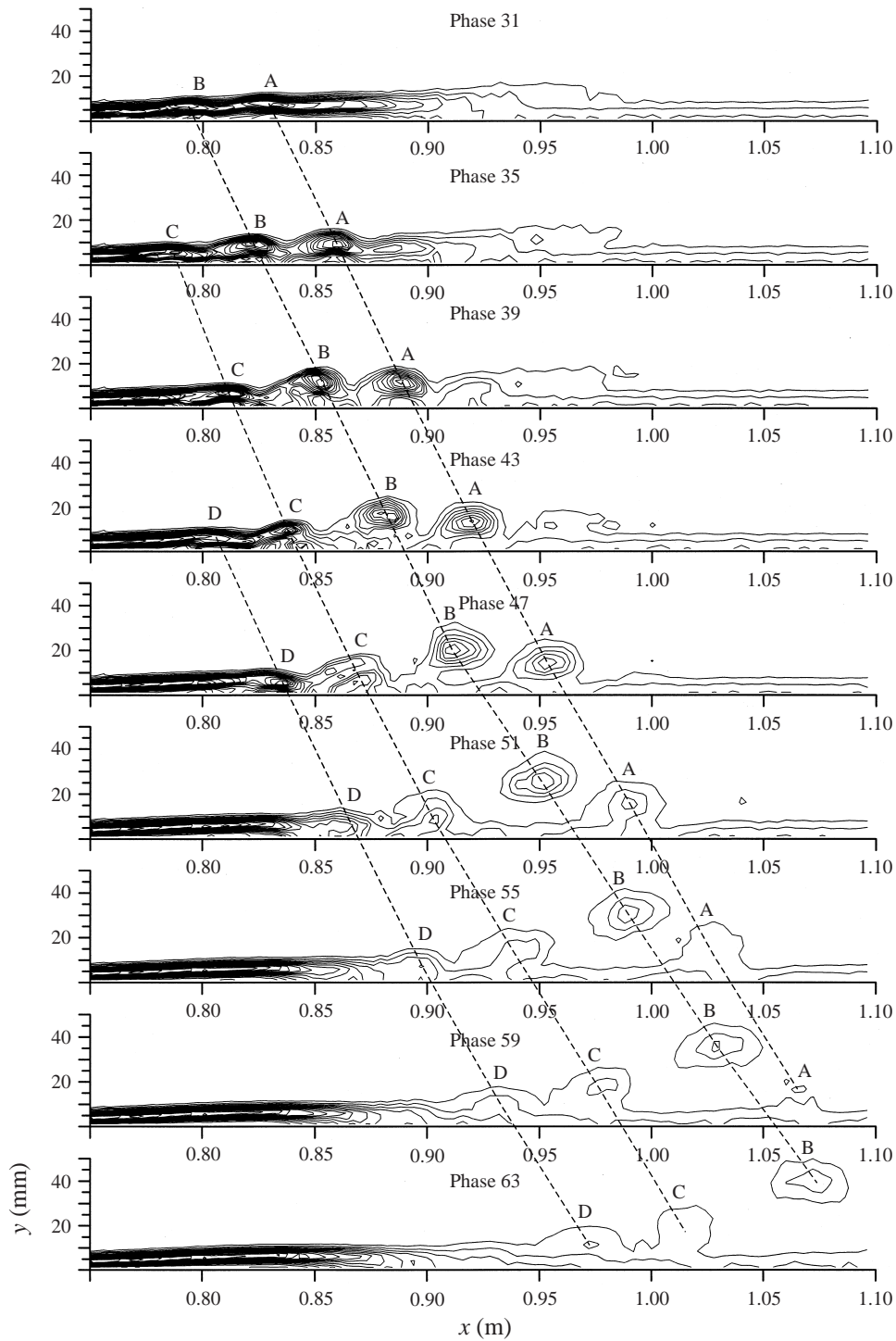


FIGURE 15. Sequence from an animation of spanwise vorticity contours on the centreline plane calculated from phase-averaged cross-wire data. Dashed lines trace the development of roll-ups into vortex loops. First roll-up (labelled A) appears short-lived, while the second roll-up (labelled B) evolves into the largest vortex loop (also see figure 16). Vortex loop B is identifiable downstream in the fully turbulent layer (see figure 20). $CI = 100 \text{ s}^{-1}$.

vorticity is mostly aligned in the spanwise direction. With subsequent development, the roll-ups develop ‘legs’ which move together and the curvature of the central region increases and accelerates away from the wall leading to the formation of elongated vortex loops. Compromises must be made in selecting the viewing angle and the single representative contour surface level for the animation sequence. Smaller loops form away from the centreline but they are difficult to ascertain. However one of the smaller off-centreline loops can be seen in figure 16, i.e. Phase 55, for $z < 0$.

As noted in §4.1, the non-dimensional frequency associated with the formation of roll-ups in the detached shear layer corresponds to $\omega^* = 0.21$, as predicted by inviscid linear stability theory. A similar result was also obtained for the two-dimensional laminar separation bubble calculations of Pauley *et al.* (1990), i.e. they found the streamwise position corresponding to the onset of two-dimensional vortex shedding to coincide with the most unstable mode predicted by linear stability theory. The connection between the two flows suggests that the evolution of the vortex loops observed in the present work represents a three-dimensional form of vortex shedding. Pauley *et al.* defined a Strouhal number based on the shedding frequency f , local free-stream velocity and the momentum thickness of the layer at separation, i.e.

$$St_\theta = \frac{f\theta_{\text{sep}}}{(U_1)_{\text{sep}}}. \quad (4.1)$$

They found the Strouhal number to be independent of the Reynolds number and the pressure gradient, i.e. $St_\theta = 6.86 \times 10^{-3}$. In the present work, a vortex shedding frequency was determined from the wavelength and propagation velocity of the centre-plane section through the three-dimensional vortex loops shown in figure 15. The corresponding Strouhal number is $St_\theta = 8.54 \times 10^{-3}$ which is about 25% larger than the invariant Strouhal number proposed by Pauley *et al.* for two-dimensional vortex shedding.

As mentioned previously, flow visualization studies have demonstrated that a turbulent spot appears to consist of an array of vortex loops. However measurements of a turbulent spot reveal only one or two large eddies, e.g. Cantwell *et al.* (1978). Evidently, the variance in the underlying detailed structure from realization to realization causes washout of data. In the present investigation, the loops appearing in the phase-averaged data downstream of the reattachment imply that the motions are more coherent. The spatial distribution of the loops in the vicinity of the reattachment may be similar to that occurring in a turbulent spot. Reynolds stress measurements are used to explore this conjecture, since the fluctuations are less susceptible to errors originating from hot-wire calibration drift and other spurious errors, compared to the total velocity measurements which must then be differentiated to calculate the total vorticity. The contribution to the Reynolds stress component normal to the test surface is shown in the horizontal plane for Phase 47 in figure 17. It is evident that the coherent motions appear to be confined within a heart-shaped boundary that is reminiscent of the corresponding boundary of a turbulent spot in a laminar boundary layer. The similarity is extraordinary since the surrounding flow is so highly unsteady in the present case of the turbulent reattachment.

As mentioned in §2.3, the Reynolds stress can be resolved into a contribution resulting from the perturbations of the phase-averaged velocities and a background component resulting from the random motion at constant phase. Both are phase-averaged quantities and the broadband Reynolds stress is given by the sum of each quantity, averaged over all phases, see (2.8). The background component originates from two sources, i.e. fluctuations due to small-scale random motions superimposed

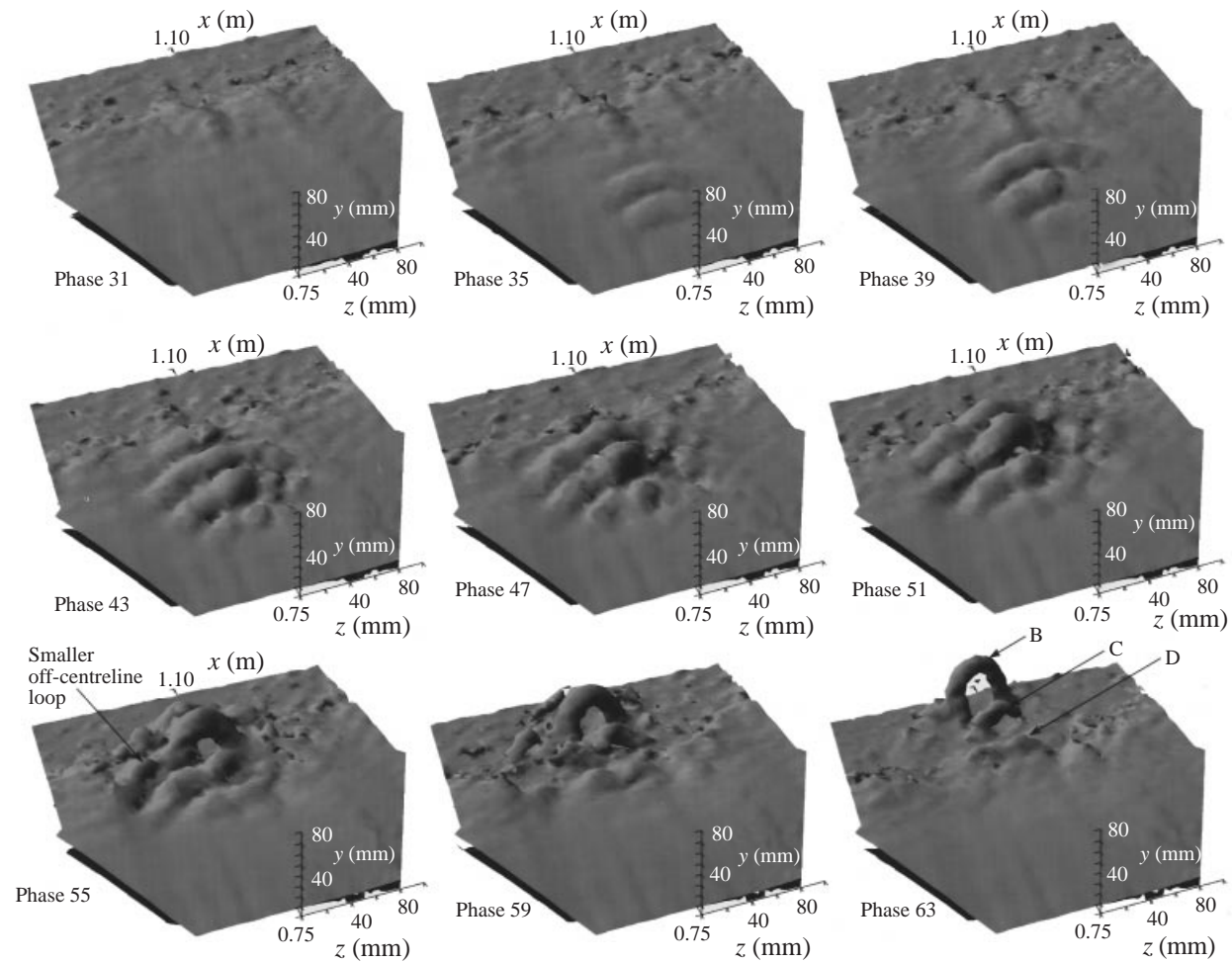


FIGURE 16. Sequence from an animation of a three-dimensional contour surface of phase-averaged vorticity magnitude ($|\Omega| = 140 \text{ s}^{-1}$) calculated from cross-wire data on true three-dimensional measurement grid of dimension $(N_x, N_y, N_z) = (45, 17, 41)$, i.e. 31 365 points. Measurements performed twice, using both orientations of the cross-wire probe to get all three velocity components. Development of three-dimensional waves on the surface and the subsequent roll-up to form vortex loops are clearly evident on the centreline. Smaller loops are also evident off centreline, e.g. $z < 0$, for Phase 55.

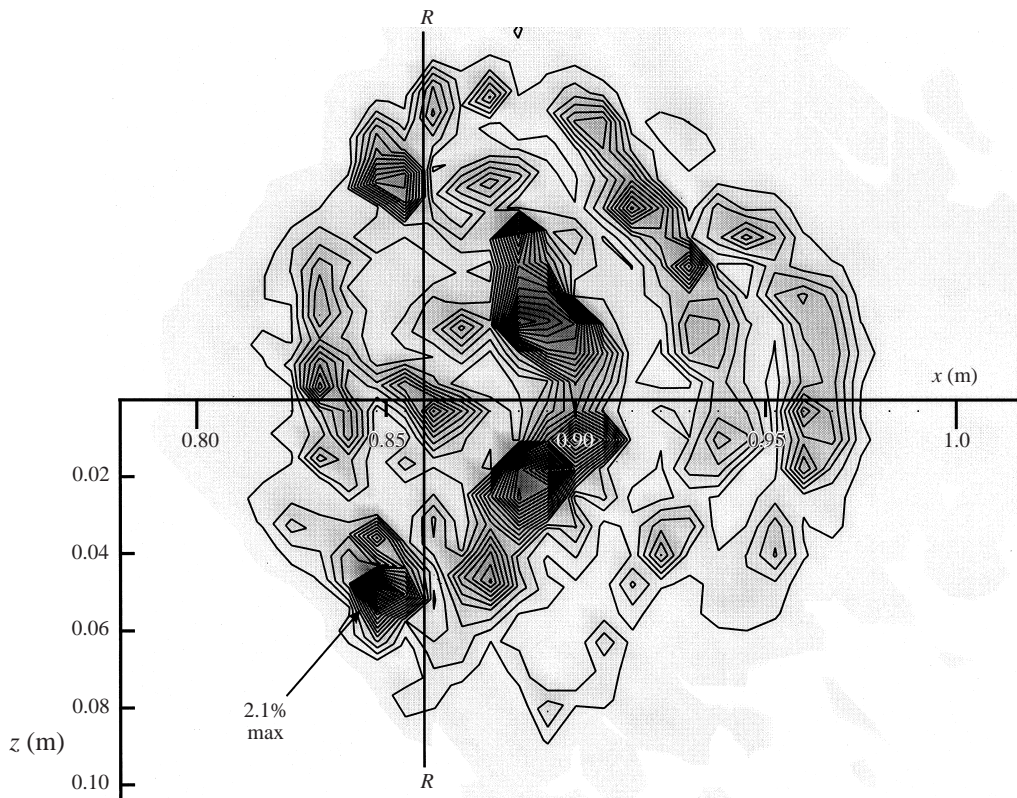


FIGURE 17. Contours of $(\bar{v}^2)^{1/2}/U_{\text{ref}}$ for Phase 47 from cross-wire data in horizontal plane $y = 10$ mm. Line labelled $R-R$ indicates reattachment point on centreline without impulsive disturbance. $CI = 0.1\%$.

on the large-scale motions; and dispersion, introduced by phase jitter and the physical differences between successive realizations. It is emphasized here again that it is not possible to differentiate between the effects of fine-scale motions and dispersion. Furthermore, it is not possible to determine whether the dispersion originates from essentially the same vortex loop appearing at slightly different positions upon each realization or whether there are small local differences between successive realizations.

Contours of the contribution and background Reynolds stresses are shown on the centreline plane in figure 18(a-f) for Phase 47. This region is just downstream of the reattachment and the corresponding spanwise vorticity contours have been taken from figure 15 and superimposed as solid black contour lines. At this stage of development, the contribution of the phase-averaged velocity components to the Reynolds stress is larger than the random background components. The contours of the contribution to the Reynolds stress components shown in figure 18(a-c) can be understood by modelling the vortex loops (and their images in the wall) with a number of straight line vortex segments and by using the Biot-Savart law for calculation of the induced velocities. The vortex segment model indicates that the largest streamwise component of the induced velocities is in the upstream direction and occurs between the legs of the vortex loops, which is consistent with the contours of $\tilde{u}^2/U_{\text{ref}}^2$ shown in figure 18(a). The larger levels associated with loop B compared

to loop A cannot be explained by the small differences in the amplitude of the vorticity magnitude. The larger levels are the result of the sharper curvature of the tip and the longer length of the legs of vortex loop B, compared to loop A, whose features are much less pronounced. The contours of the contribution to the Reynolds stress in the direction normal to the wall, $\tilde{v}^2/U_{\text{ref}}^2$, are shown in figure 18(c). These contours are also consistent with the vortex segment model. However the distribution is asymmetrical with respect to the centre of cross-section through each loop since there is some cancellation of the induced velocity between the loops. The contribution to the Reynolds shear stress $\tilde{u}\tilde{v}/U_{\text{ref}}^2$ can be divided into four quadrants based on the sign of induced velocities as shown in figure 18(b). The quadrants are spatially related to the distribution of the spanwise vorticity as shown by the regions labelled Q1 to Q4 for loop B in figure 18(b). The induced velocities from the legs of the loops lead to the 2nd and 3rd quadrants (closest to the wall) being dominant. Note the rather large positive shear stress amplitude $\tilde{u}\tilde{v}/U_{\text{ref}}^2$ associated with Q3.

The background Reynolds stresses resulting from fluctuations which are random with respect to the total phase-averaged velocities are shown in figure 18(d–f) and they are more uniformly distributed than the periodic contribution components. Large levels of the streamwise component $\langle u''^2 \rangle / U_{\text{ref}}^2$ are observed to extend from regions of concentrated vorticity down towards the wall in figure 18(d) corresponding to the region between the legs of the vortex loops. The distribution of the background component of the shear stress $\langle u''v'' \rangle / U_{\text{ref}}^2$ in figure 18(e) appears to be similar to the streamwise component. The distribution is almost entirely negative except for a narrow region of positive amplitude which can be found in the vicinity of $x = 0.9$ m, i.e. between the legs of vortex loop A. In contrast, the background component normal to the wall $\langle v''^2 \rangle / U_{\text{ref}}^2$ is more locally concentrated as shown in figure 18(f).

If phase jitter were significant, then local maxima in the background Reynolds stress might be expected to coincide with large gradients in the contribution to the corresponding Reynolds stress component. Inspection of figure 18(a–f) suggests that this does not appear to be the case at this stage of development. For example, in figure 18(c), large gradients of $\tilde{v}^2/U_{\text{ref}}^2$ not only correspond to the centre of $\langle v''^2 \rangle / U_{\text{ref}}^2$ but also extend upstream and downstream. However, the local maxima in the background component $\langle v''^2 \rangle / U_{\text{ref}}^2$ are confined to the region of concentrated vorticity as shown in figure 18(f). These observations suggest that at this stage of development it is likely that the background Reynolds stress distribution can be attributed to fine-scale motions associated with the vortex loops.

4.3. Persistence of vortex loops in the downstream turbulent boundary layer

Phase-averaged cross-wire data (UV -orientation only) have been measured in a number of sequential centreline planes in the turbulent boundary layer downstream of the reattachment. The results from each grid have been combined to form a composite data set on a single grid. Cross-wire data (using both probe orientations) have also been measured in a number of spanwise planes. The increased phase jitter and the presence of fine-scale turbulent motions cause the magnitude of the phase-averaged velocity perturbations to be much smaller in the downstream turbulent boundary layer, e.g. the maximum r.m.s. amplitude of the phase-averaged streamwise fluctuations at $x = 2.0$ m is an order of magnitude less than the peak value observed in the reattachment region.

It is well known that the flow pattern generated by a velocity vector field depends on the velocity of the observer. It is difficult to select an observer velocity such that the effect of the temporal mean velocity gradient at the wall is reduced to an insignificant

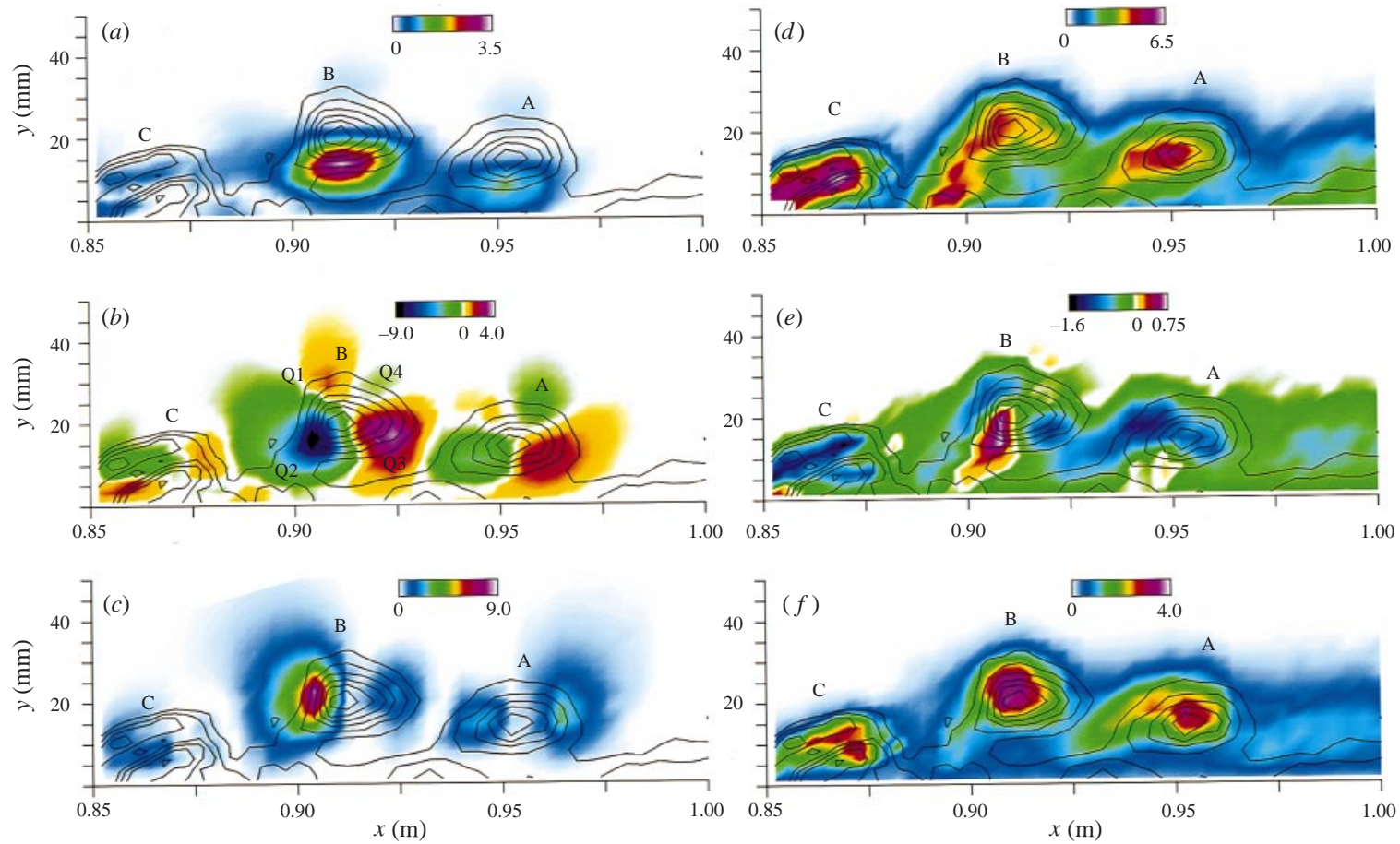


FIGURE 18. Colour contours of Reynolds stress in centreline plane for Phase 47. Contribution by phase-averaged velocity fluctuations, (a) $\tilde{u}^2/U_{\text{ref}}^2$, (b) $\tilde{u}\tilde{v}/U_{\text{ref}}^2$ and (c) $\tilde{v}^2/U_{\text{ref}}^2$. Background Reynolds stress from fluctuations which are random with respect to the phase-averaged velocity components, (d) $\langle u''^2 \rangle / U_{\text{ref}}^2$, (e) $\langle u''v'' \rangle / U_{\text{ref}}^2$ and (f) $t\langle v''^2 \rangle / U_{\text{ref}}^2$. Solid black contour lines of phase-averaged spanwise vorticity are provided for reference showing cross-sections through loops labelled A, B, and C (from figure 15). $CI = 100 \text{ s}^{-1}$. Legends for colour contours indicate percent.

level. Furthermore, the small magnitude of the phase-averaged perturbations adds to the difficulties of interpretation of the total phase-averaged velocity vector flow field since the temporal mean velocity components are considerably larger. Small measurement errors in the temporal mean flow quantities can introduce considerable scatter since the errors can easily be of comparable size to the phase-averaged perturbations.

Representative phase-averaged velocity perturbation vectors are shown in figure 19(a). The flow pattern generated by the velocity perturbation vector field avoids many of the difficulties mentioned above, but it is difficult to attach precise meaning to the flow pattern. Vorticity is a quantity that is independent of the velocity of the observer. The corresponding contours of the phase-averaged spanwise vorticity perturbations are shown in figure 19(b). The overall shape of the spanwise vorticity perturbation contours changes very little for different streamwise positions. However, the reduced magnitude of the phase-averaged perturbations and the small measurement errors in the temporal mean velocity components have the combined effect of introducing considerable scatter into the contours of the total phase-averaged vorticity. The scatter increases with downstream distance. Corresponding total phase-averaged spanwise vorticity contours are shown in figure 19(c). The effects mentioned above are not severe at this streamwise position, but by $x = 2.0$ m, the contours of phase-averaged total vorticity show considerable scatter, while the contours of the phase-averaged vorticity perturbations have much the same appearance as those further upstream.

The small rate of change of the vorticity perturbation contours with streamwise distance suggests that Taylor's hypothesis for phase (pseudo-flow visualization) can be applied to the spanwise grids to generate three-dimensional data sets that are representative of the true spatial three-dimensional data (which have not been measured). The total phase-averaged vorticity contours obtained by applying Taylor's hypothesis for phase to the centreline data of the spanwise plane located at $x = 1.5$ m are shown in figure 19(d). A uniform scaling was used for transforming ϕ to x which was determined from a local linear fit to the phase of the peak values of $\tilde{u}(y, z)$ as a function of x . The reasonably good correspondence between the contours in figure 19(c,d) indicates that the three-dimensional data generated from the measurements in the spanwise planes provide a reasonably close approximation to the true spatial three-dimensional data.

Complete three-dimensional, i.e. $(\langle U \rangle, \langle V \rangle, \langle W \rangle)$, velocity vector fields have been generated using Taylor's hypothesis applied to the spanwise planes located at $x = 1.0, 1.25, 1.5$ and 2.0 m. Contour surfaces of the corresponding total phase-averaged vorticity magnitude and the phase-averaged vorticity perturbations are shown in figure 20(a-h). Each figure also contains colour contours on the centreline plane and on a plane parallel to the wall. The wall distance of the plane parallel to the wall was chosen to aid interpretation of the three-dimensional data.

The perturbation, figure 20(a), and total, figure 20(b), phase-averaged vorticity magnitude distribution at $x = 1.0$ m provide additional feedback on the accuracy of Taylor's hypothesis for generating three-dimensional flow fields from the spanwise planar measurements. The greatest deviation from the true spatial distribution is expected to occur at this position because the streamwise derivatives of flow quantities are the largest here. The flow field generated from this spanwise plane overlaps the true spatial measurements in figure 15 and figure 16 (e.g. Phase 55) and a comparison reveals that the salient features have been reproduced.

Further downstream, at $x = 1.25$ m, the contours of vorticity magnitude in figure

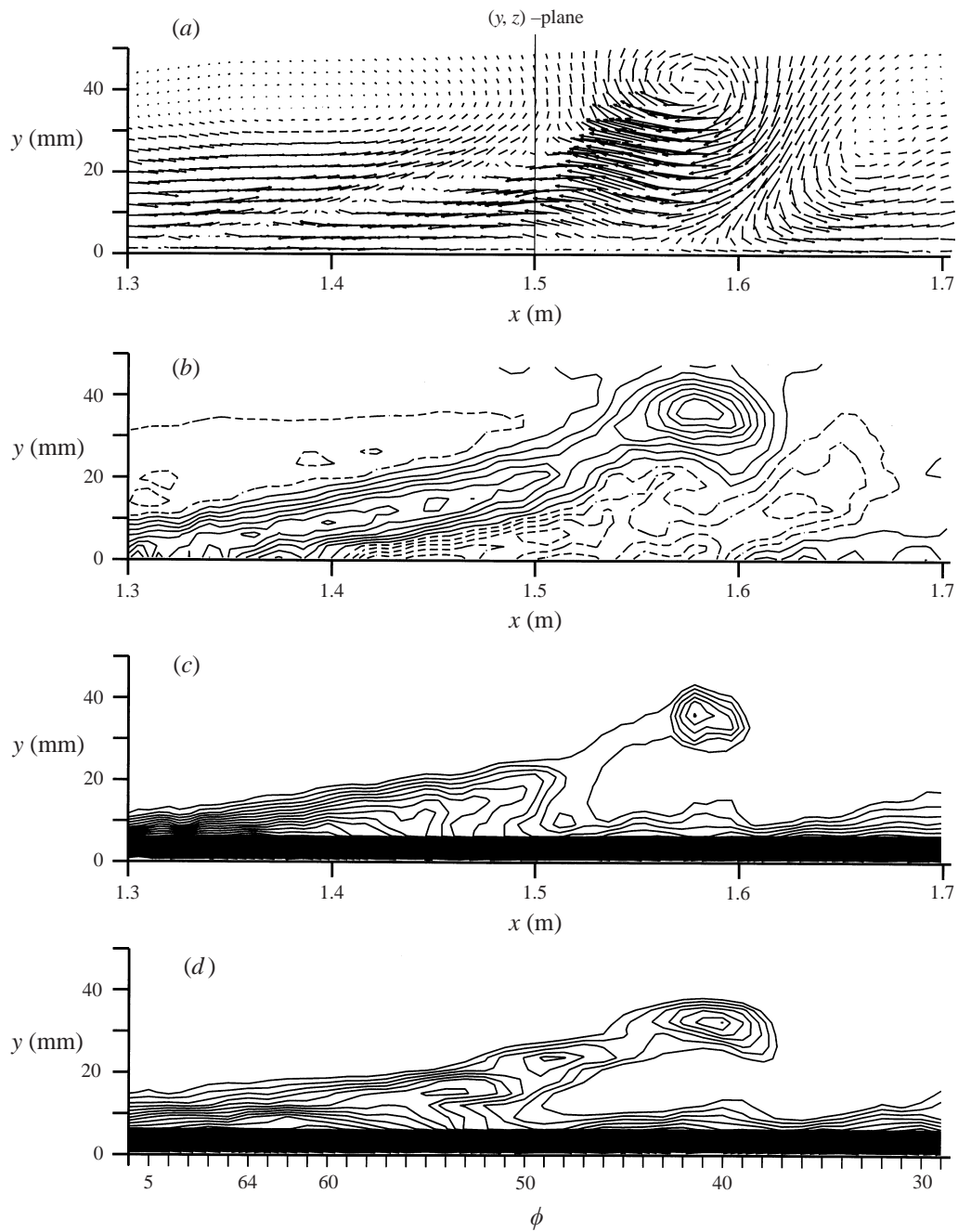


FIGURE 19. Centreline plane in turbulent boundary layer. (a) Phase-averaged velocity perturbation vector field. (b) Corresponding spanwise vorticity perturbation contours, ω_z . Solid lines are negative and dashed lines positive levels. $CI = 5 \text{ s}^{-1}$. Contours in the range, $-15 \text{ s}^{-1} < \omega_z < 15 \text{ s}^{-1}$ not shown owing to scatter. (c) Corresponding total phase-averaged spanwise vorticity contours, Ω_z . $CI = -5 \text{ s}^{-1}$. (d) Total phase-averaged spanwise vorticity contours, Ω_z , derived by applying Taylor's Hypothesis for phase to the centreline data measured on the spanwise plane at $x = 1.5$ m. $CI = -5 \text{ s}^{-1}$.

20(c,d) clearly show the presence of a vortex loop which can be traced back to the dominant loop that emerges in the reattachment region upstream. This loop is labelled B in figure 15. Both the perturbation and total vorticity contour surfaces indicate that the vorticity is more concentrated in the outer region of the loop. The legs of the loop extend down close to the wall but this is not visible for the chosen contour surface level. There are two additional noteworthy regions of concentrated vorticity present in the total vorticity magnitude distribution in figure 20(d). The first region is located near the wall in the vicinity of the centreline between the legs of the loop. It should be emphasized that this region is distinctly separate from the legs of the loop. The local 'upwelling' of the concentrated vorticity at the wall can be explained in terms of the induced velocities generated by the loop. The second noteworthy region consists of a pair of upwellings of near-wall vorticity symmetrically displaced from the centreline downstream of the loop. It is difficult to explain these upwellings in terms of velocities induced by the vortex loop. These regions may be related to remnants of the first distinct roll-up, labelled A, in the reattachment region.

The loop and the two regions of concentrated vorticity can also be seen in the total vorticity contours at $x = 1.5$ m in figure 20(f). The local upwelling of near-wall vorticity between the legs can be more clearly seen in the centreline plane of the true spatial contours of figure 19(c) in the vicinity of $x = 1.4$ m. As mentioned previously, the phase-averaged velocity perturbations are considerably weaker at $x = 2.0$ m and considerable scatter in the total vorticity contours is apparent as shown in figure 20(h). However the loop is still clearly visible in the perturbation contour surface shown in figure 20(g).

It is emphasized once again that the cross-wire data have not been interpolated and that smoothing has not been applied to the phase-averaged velocities to reduce the scatter introduced by the differentiation to calculate the vorticity magnitude. Given these limitations, and the reduced magnitude of the phase-averaged perturbations, it is extraordinary that the phase-averaged vortex loop formed in the reattachment region retains its identity some 20 boundary layer thicknesses downstream in the fully turbulent boundary layer. Given the rate of decay of the phase-averaged perturbations, it is evident that the loop would persist in the phase-averaged data for an even greater streamwise distance if a longer test section were available.

5. Concluding remarks

It is possible that the most amplified modes of the wave packet could have much smaller amplitude than the damped modes, which would explain the initial decay of the amplitude with streamwise distance in the APG while the layer is attached. However, it is more probable that the impulsive disturbance excites a uniform spectrum of spanwise modes, i.e. the assumption used by Gaster (1975). Consequently, the initial decay suggests that the layer is viscously stable with respect to small-magnitude disturbances (such as Tollmien–Schlichting waves) while it remains attached. The growth in wave amplitude that occurs after separation is due to an inviscid Kelvin–Helmholtz instability in the detached shear layer. The non-dimensional frequency associated with the appearance of the cat's eye pattern corresponds to the most amplified mode predicted by linear stability theory for the parallel flow of a free shear layer in a ZPG. It is therefore appropriate to refer to the disturbance as a Kelvin–Helmholtz wave packet, analogous to the Tollmien–Schlichting wave packet studied by Gaster (1975) and Gaster & Grant (1975).

The dispersion and rapid growth in amplitude associated with the Kelvin–Helmholtz

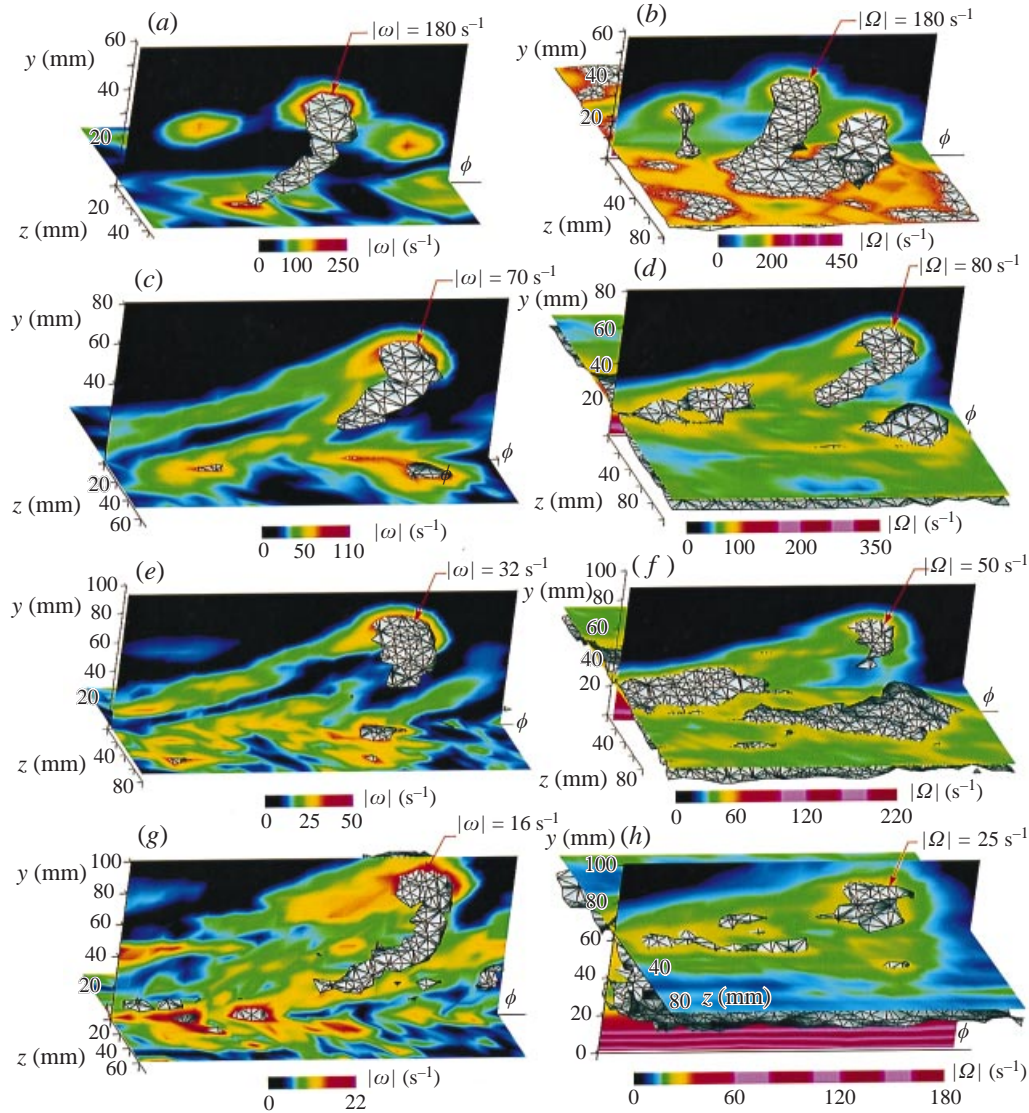


FIGURE 20. Contour surface and colour contours of vorticity magnitude on the centreline plane and on a plane parallel to wall. Vorticity magnitude calculated from the three-dimensional velocity field derived by applying Taylor's hypothesis for phase to cross-wire measurements in spanwise planes (i.e. pseudo-flow visualization). Vortex loop labelled B in figure 15 persists in the downstream turbulent boundary layer. (a), (c), (e) and (g) Vorticity magnitude perturbations; (b), (d), (f) and (h) total vorticity magnitude. Location of spanwise planes: (a), (b) at $x = 1.0$ m, (c), (d) at $x = 1.25$ m, (e), (f) at $x = 1.5$ m, and (g), (h) at $x = 2.0$ m.

wave packet lead to the formation of roll-ups which ultimately evolve into large-scale vortex loops in the vicinity of the reattachment. When the disturbance is present in the layer, the reattachment occurs only a little further upstream as indicated by the streamwise C_p distributions and the broadband Reynolds stress distributions. The passing frequency of the phase-averaged disturbance calculated from the wavelength and phase velocity is very closely the same as the centre frequency of a very narrow band of elevated energy level in the power spectra observed without

the disturbance. The same exponential growth rate occurs for the wave packet and the background disturbances. Therefore it is tempting to conclude that in general the phase-averaged observations are representative of instabilities arising from three-dimensional background disturbances present in the flow. However other factors must be considered to determine the degree to which the phase-averaged observations are representative of the unsteady phenomena that occur in the detached shear layer.

The experiments described by Kozlov (1984) and Dovgal *et al.* (1986) demonstrate that two-dimensional instability waves can form in the detached shear layer under the excitation of acoustic waves originating in the far field, e.g. sound from a speaker located in the wind tunnel diffuser. Therefore, environmental noise in the test section could be responsible for a large proportion of the unsteadiness leading to the reattachment in the present investigation. The spanwise non-uniformity observed in the reattachment region, as shown in figure 8(a), does not preclude the occurrence of two-dimensional instability waves. It is possible that three-dimensional secondary instabilities could be associated with the initially two-dimensional waves in the region of nonlinear growth, just prior to the reattachment, i.e. analogous to the spanwise waviness associated with secondary instability of Tollmien–Schlichting waves in a Blasius boundary layer prior to nonlinear breakdown. However, Kozlov (1984) and Dovgal *et al.* (1986) report that large-amplitude acoustic waves (e.g. 100 dB) are typically required to generate waves of significant amplitude in detached shear layers. Furthermore, the detached shear layer is receptive only to a relatively narrow band of frequencies. The background noise level at the entrance to the test section in the present investigation is estimated to be in the range of 20 dB to 30 dB based on measurements using a calibrated Bruel & Kjaer microphone and amplifier. The relative amplitude of the microphone signal is quite small in a band corresponding to the blade passing frequency of 72 Hz, while the corresponding spectra of the signal from a hot wire located in the detached shear layer contains a narrow band of elevated amplitude with a centre frequency of 87 Hz. These measurements suggest that it is unlikely that instabilities associated with two-dimensional waves originating from acoustic disturbances are responsible for the peak in the hot-wire spectra. Therefore, purely two-dimensional waves probably do not play a significant role in the reattachment in the present configuration and the development of three-dimensional phenomena is likely to be important.

The contribution to the Reynolds stress component normal to the test surface shown in figure 8(c) demonstrates how vortex loops can introduce three-dimensional characteristics into the mean flow. The dominant flow structure in the reattachment region may consist of vortex loops similar to the phase-averaged observations in figure 16. However, if the spanwise variation in the contours of the total broadband Reynolds stress shown in figure 8(a) is to be attributed to formation of vortex loops, then the probability of the formation of a loop at a given spanwise position would have to be non-uniform. Such a statistically non-uniform distribution for the appearance of vortex loops in the reattachment region may be somehow associated with the spanwise variations in the layer thickness upstream of the separation that are implied by the streaks appearing in the contours in figure 7(a). However, in the present work, no attempt has been made to establish a direct connection between the mean flow non-uniformity upstream of the separation and downstream of the reattachment.

The coupling between the mean flow and instabilities appearing in separated flows is noted in the review by Dovgal *et al.* (1994). Larger disturbance levels in the detached shear layer lead to a shorter bubble in the mean flow sense. The reduced length of

the bubble when the disturbance is present is evident in the C_p distribution shown in figure 2. The contours in figure 8(a, b) are also consistent with the formation of a shorter bubble when the disturbance is present since larger amplitudes are observed at a given position on the centreline upstream of the reattachment. For the case without the disturbance, in figure 8(a), the spanwise positions of regions of elevated amplitude upstream of the reattachment correlate well with the spanwise positions of the peak amplitude levels downstream of the reattachment. However, for the case with the disturbance, in figure 8(b), the broadband amplitude level at a given position on the centreline upstream of the reattachment is larger, while the peak amplitude level downstream of the reattachment is smaller, than when the disturbance is not present. This observation is difficult to explain and may imply that other phenomena also play an important role in the reattachment process.

The evolution of vortex loops observed in the present work could represent a three-dimensional form of vortex shedding, analogous to the two-dimensional vortex shedding in the computations by Pauley *et al.* (1990). It is clear from their work that the vortex shedding is not directly associated with the bubble, but rather that the separation bubble is responsible for the establishment of a free-shear layer and that the shedding process is initiated by an inviscid instability associated with the inflection point which lies outside the bubble. In both flows, the frequency of the instability appearing in the detached shear layer corresponds to the most amplified mode predicted by inviscid linear stability theory. Furthermore, the difference between the Strouhal numbers for the two-dimensional and three-dimensional shedding is fairly small (based on the parameters of Pauley *et al.*). Overall, there is a similarity between the vortex shedding observed by Pauley *et al.* and that behind a blunt two-dimensional body, such as a cylinder, in so far as both result in limit-cycle oscillations. Based on this observation, the two-dimensional vortex shedding observed by Pauley *et al.* is most probably the result of an absolute instability, in terms of the classification offered by Huerre & Monkewitz (1990).

One property of an absolute instability is that its manifestation at a given streamwise position remains after the disturbance has been removed. For example, the vortex shedding behind a two-dimensional cylinder will persist indefinitely once it has been excited by an impulsive disturbance (for a Reynolds number based on diameter greater than 40). Classification of the phenomena observed by Pauley *et al.* (1990) is not straightforward since the impulsive disturbance (i.e. application of the APG) is responsible for establishing the mean flow and it could also be responsible for exciting the instability in the detached shear layer. On the other hand, the formation of three-dimensional vortex loops generated by the impulsive disturbance in the present work appears to be transient in the sense that the formation of the loops does not persist indefinitely, and another application of the impulsive disturbance is required for their generation. In terms of the nomenclature of Huerre & Monkewitz (1990), the three-dimensional vortex shedding process could be classified as a convective instability. Further work is required to determine whether these hypotheses are correct, i.e. that three-dimensional vortex shedding can be classified as a convective instability, while the corresponding two-dimensional vortex shedding in the same flow should be viewed as an absolute instability.

The dominant phase-averaged vortex loop formed in the reattachment region retains its identity some 20 boundary layer thicknesses downstream in the fully turbulent boundary layer. The loop would persist for an even greater distance if a longer test section were available. The phase-averaged velocity field and Reynolds stress distribution surrounding the vortex loop in the turbulent boundary layer should be of

some interest since many workers have proposed that vortex loops are the dominant coherent structure underlying turbulent boundary layers in general.

The flow will provide a challenging test case for computational studies. The Falkner & Skan velocity profile in the FPG provides a simple and convenient inlet boundary condition. Yet the satisfactory treatment of the exceptionally large velocity fluctuations and the instantaneous flow reversals in the reattachment region will be a formidable task.

It should be noted that there are some similarities with the process of shear-layer breakdown and the formation of vortex loops that occur in attached boundary layers. For example, secondary instability of boundary layers, Herbert (1988), involves the onset of waviness in initially two-dimensional Tollmien–Schlichting waves and the subsequent nonlinear breakdown leads to the formation of smaller detached shear layers and vortex loops due to inflectional instability. Unlike the detached shear layer above the separation bubble, considerable detail is known about the processes occurring in attached boundary layers. For example, Kachanov (1994) describes various classifications such as *K*-type breakdown, where the loops or Λ -vortices are aligned, and *N*-type breakdown, where the Λ -vortices are staggered.

The APG imposed by suction through the ceiling of the duct in the study of Pauley *et al.* (1990) is different to the present configuration, since the APG is localized and of finite length. The flow experiences a ZPG downstream of the bubble which allows the formation of a steady bubble to occur at low Reynolds numbers. In contrast, the APG in the present configuration extends to the end of the test section and the large stream-wise extent of the detached shear layer almost certainly precludes the possibility of obtaining a steady separation bubble. Even if the Reynolds number were substantially reduced and even if the background disturbances were reduced to immeasurably small levels, it is almost certain that the disturbances would still have the opportunity to grow to large enough amplitudes to initiate the reattachment. In order to clearly differentiate between competing effects, an experimental configuration is required where the reattachment is laminar. Small finite-amplitude two-dimensional disturbances (e.g. vibrating ribbon) and three-dimensional disturbances (e.g. impulsive and harmonic point sources) could then be deliberately introduced in a controlled manner, and any changes in the characteristics of the separation bubble could then be directly attributed to the presence of the disturbances. A precise one-to-one correspondence might then be established between observation, theory and computation, along the lines that have led to advances in understanding transition of the Blasius boundary layer.

The properties of the turbulent boundary layer downstream of the reattachment show considerable differences to the turbulent boundary layer downstream in the study reported by Spalart & Watmuff (1993). For example, the peak values of the Reynolds shear stress are located in the central portion of the layer downstream of the region reported by Spalart & Watmuff (see figure 7 of Watmuff 1995) while the peak values are located close to the wall in the layer downstream of the reattachment considered in the present paper. The differences are interesting because the same unit Reynolds number and pressure distribution are imposed, i.e. the differences must be attributed to upstream history effects. Both flows will provide a significant challenge for advanced code development and for the testing of turbulence models. It is anticipated that a comparison will be published separately showing the widely different characteristics of the two turbulent boundary layers.

This experiment was supported by and performed in the Fluid Mechanics Laboratory (FML) at NASA Ames Research Center. The author would like to thank the

referees and Murray Tobak for the careful reviews of the manuscript. The project was started during the last two months of support for the author by the Center for Turbulence Research of NASA Ames Research Center and Stanford University. The measurements were completed while the author was supported by the MCAT Institute under Cooperative Agreement NCC2-698. Much of the analysis of the data were performed while the author was supported by the MCAT Incorporated under Contract Number NAS2-14109.

REFERENCES

- CANTWELL, B. J. & COLES, D. 1983 An experimental study of entrainment and transport in the turbulent near wake of a circular cylinder. *J. Fluid Mech.* **136**, 321–374.
- CANTWELL, B. J., COLES, D. & DIMOTAKIS, P. 1978 Structure and entrainment in the plane of symmetry of a turbulent spot. *J. Fluid Mech.* **87**, 641–672.
- COHEN, J., BREUER, K. S. & HARITONIDIS, J. H. 1991 On the evolution of a wave packet in a laminar boundary layer. *J. Fluid Mech.* **225**, 575–606.
- CURLE, N. & SKAN, S. W. 1957 Approximate methods for predicting separation properties of laminar boundary layers. *Aero. Q.* **8**, 257–268.
- DOBBINGA, E., INGEN, J. L. VAN & KOOI, J. W. 1972 Some research on two-dimensional separation bubbles. *AGARD CP-102*, paper 2.
- DOVGAL, A. V. & KOZLOV, V. V. 1990 Hydrodynamic instability and receptivity of small scale separation regions. In *Laminar-Turbulent Transition, Proc. IUTAM Symp.*, pp. 523–531. Springer.
- DOVGAL, A. V., KOZLOV, V. V. & MICHALKE, A. 1994 Laminar boundary layer separation: instability and associated phenomena. *Prog. Aerospace Sci.* **30**, 61–94.
- DOVGAL, A. V., KOZLOV, V. V. & SIMONOV, O. A. 1986 Experiments on hydrodynamic instability of boundary layers with separation. In *Boundary Layer Separation, Proc. IUTAM-Symp., London*, pp. 109–130. Springer.
- GASTER, M. 1966 The structure and behaviour of laminar separation bubbles. *AGARD CP-4*, pp. 813–854.
- GASTER, M. 1975 A theoretical model of a wave packet in the boundary layer on a flat plate. *Proc. R. Soc. Lond. A* **347**, 271–289.
- GASTER, M. & GRANT, I. 1975 An experimental investigation of the formation and development of a wave packet in a laminar boundary layer. *Proc. R. Soc. Lond. A* **347**, 253–269.
- HERBERT, T. 1988 Secondary instability of boundary layers. *Ann. Rev. Fluid Mech.* **20**, 487–526.
- HUERRE, P. & MONKEWITZ, P. A. 1990 Local and global instabilities in spatially developing flows. *Ann. Rev. Fluid Mech.* **22**, 473–537.
- INGER, G. R. 1987 Spanwise-periodic 3-D disturbances in the wake of a slightly stalled wing. *AIAA Paper* 87-0456.
- JONES, B. M. 1934 Stalling. *J. R. Aero. Soc.* **38**, 747–770.
- KACHANOV, Y. S. 1994 Physical mechanisms of boundary layer transition. *Ann. Rev. Fluid Mech.* **26**, 411–482.
- KOZLOV, V. V. 1984 Interrelation of the flow separation and stability. In *Laminar-Turbulent Transition, Proc. IUTAM-Symp.*, pp. 349–358. Springer.
- LIGHTHILL, M. J. 1963 Boundary layer theory. In *Laminar Boundary Layers* (ed. L. Rosenhead), pp. 46–113. Oxford.
- MACK, L. M. 1984 Boundary Layer stability theory. In *Special Course on Stability and Transition of Laminar Flow. AGARD Rep.* 709.
- MCCULLOUGH, G. B. & GAULT, D. E. 1951 Examples of three representative types of airfoil-section stall at low speed. *NACA TN* 2502.
- MICHALKE, A. 1964 On the inviscid instability of the hyperbolic-tangent velocity profile. *J. Fluid Mech.* **19**, 543–556.
- MONKEWITZ, P. A. & HUERRE, P. 1982 Influence of the velocity ratio on the spatial instability of mixing layers. *Phys. Fluids* **25**, 1137–1143.
- MORKOVIN, M. V. 1984 Bypass transition to turbulence and research desiderata, Transition in Turbines. *NASA Conf. Publ.* 2386, pp. 161–204.

- OBREMSKI, H. J., MORKOVIN, M. V. & LANDAHL, M. 1969 A portfolio of stability characteristics of incompressible boundary layers. *AGARDograph* 134.
- PAULEY, L. L. 1994 Response of two-dimensional separation to three-dimensional disturbances. *Trans. ASME: J. Fluids Engng* **116**, 433–438.
- PAULEY, L. L., MOIN, P. & REYNOLDS, W. C. 1990 The structure of two-dimensional separation. *J. Fluid Mech.* **220**, 397–411.
- PEAKE, D. J. & TOBAK, M. 1980 Three-dimensional interactions and vortical flows with emphasis on high speeds. *AGARDograph* 252.
- PERRY, A. E., LIM, K. L. & HENBEST, S. M. 1987 An experimental study of the turbulence structure of smooth- and rough-wall boundary layers. *J. Fluid Mech.* **177**, 437–466.
- PERRY, A. E., LIM, T. T. & TEH, E. W. 1981 A visual study of turbulent spots. *J. Fluid Mech.* **104**, 387–405.
- PERRY, A. E. & WATMUFF, J. H. 1981 Phase-averaged large-scale structures in three-dimensional turbulent wakes. *J. Fluid Mech.* **103**, 33–51.
- REYNOLDS, W. C. & HUSSAIN, A. K. M. F. 1972 The mechanics of an organised wave in turbulent shear flow. Part 3. Theoretical models and comparison with experiments. *J. Fluid Mech.* **54**, 263–288.
- ROSHKO, A. & THOMKE, G. J. 1966 Observations of turbulent reattachment behind an axisymmetric downstream-facing step in supersonic flow. *AIAA J.* **4**, 975–980.
- SPALART, P. & WATMUFF, J. H. 1993 An experimental and numerical study of a turbulent boundary layer with pressure gradients. *J. Fluid Mech.* **249**, 337–371.
- THWAITES, B. 1949 Approximate calculation of the laminar boundary layer. *Aero. Q.* **14**, 61–85.
- VILLERMAUX, E. 1998 On the role of viscosity in shear instabilities. *Phys. Fluids* **10**, 368–373.
- WATMUFF, J. H. 1995 High-speed real-time processing of cross-wire data. *Expl Thermal Fluid Sci. J.* **10**, 74–75.
- WATMUFF, J. H., PERRY, A. E. & CHONG, M. S. 1983 A flying hot-wire system. *Exps. Fluids* **1**, 63–71.